Advanced Materials for Energy Conversion and Storage: Low-Temperature, Solid-State Conversion Reactions of Cuprous Sulfide and the Stabilization and Application of Titanium Disilicide as a Lithium-Ion Battery Anode Material

Author: Zachary Ian Simpson

Boston College

The Graduate School of Arts and Sciences

Department of Chemistry

ADVANCED MATERIALS FOR ENERGY CONVERSION AND STORAGE: LOW-TEMPERATURE, SOLID-STATE CONVERSION REACTIONS OF CUPROUS SULFIDE AND THE STABILIZATION AND APPLICATION OF TITANIUM DISILICIDE AS A LITHIUM-ION BATTERY ANODE MATERIAL

a thesis

by

ZACHARY IAN SIMPSON

submitted in partial fulfillment of the requirements

for the degree of

Master of Science

May 2013

Title:

Advanced materials for energy conversion and storage: low-temperature, solid-state conversion reactions of cuprous sulfide and the stabilization and application of titanium disilicide as a lithium-ion battery anode material.

Author: Zachary I. Simpson

Advisor: Professor Dunwei Wang

Abstract:

In this work, we present our findings regarding the low-temperature, solid-state conversion of Cu_2S nanowires to Cu_2S/Cu_5FeS_4 rod-in-tube structures, Cu_2S/ZnS segmented nanowires, and a full conversion of Cu_2S nanowires to ZnS nanowires. These conversion reactions occur at temperatures as low as 105 °C, a much lower temperature than those required for reported solid-state reactions. The key feature of the Cu_2S nanowires that enables such low conversion temperatures is the high ionic diffusivity of the Cu^+ within a stable S sublattice.

The second portion of this work will focus on the oxide-stabilization and utilization of $TiSi_2$ nanonets as a lithium-ion battery anode. This nanostructure, first synthesized in our lab, was previously demonstrated to possess a lithium storage capacity when cycled against a metallic Li electrode. However, with subsequent lithiation and delithiation cycles, the $TiSi_2$ nanonet structure was found to be unstable. By allowing a thin oxide layer to form on the surface of the nanonet, we were able to improve the capacity retention of the nanonets in a lithium-ion half-cell; 89.8% of the capacity of the oxide-

coated $TiSi_2$ was retained after 300 cycles compared to 62.3% of the capacity of as-synthesized $TiSi_2$ nanonets after 300 cycles. The layered structure of C49 $TiSi_2$ exhibited in the nanonets allows for a specific capacity greater than 700 mAh g^{-1}, and the high electrical conductivity of the material in conjunction with the layered structure confer the ability to cycle the anode at rates of up to 6C, i.e., 10 minute charge and discharge cycles, while still maintaining more than 75% of the capacity at 1C, i.e., 1 hour charge and discharge cycles.

Table of Contents

Abbreviations

ALD	atomic layer deposition
CVD	chemical vapor deposition
ED	electron diffraction
EDS	energy dispersive X-ray spectroscopy
EELS	electron energy loss spectroscopy
EIS	electrochemical impedance spectroscopy
NN	nanonet
NR	nanorod
NW	nanowire
RIT	rod-in-tube
SEI	solid electrolyte interface
SEM	scanning electron microscopy
TEM	transmission electron microscopy
XRD	X-ray diffraction

Acknowledgements

First, I would like to thank Prof. Dunwei Wang for everything he has done for me throughout the years and for being my advisor. I came to Boston College unsure of my direction, but Dunwei's passion for science and his enthusiasm for research encouraged me to follow the path that I have taken. I thank him for his guidance, his faith in me by accepting me to the group, and for his advice and mentorship during my research undertakings.

I extend my gratitude to the readers of my thesis for the valuable time they have set aside to read and criticize this work in order to make it the best that it can possibly be. Thank you also for the scientific insight and guidance you have provided me throughout the years.

Thank you to the Wang lab members, both past and present. Thank you especially to Matt and Andrew for welcoming me to the lab and making it a great place to be. Thank you to Yongjing for keeping the lab in order for all of us during your stay. Thank you to Xiaohua for your knowledge, insight, and guidance during my time on the Cu_2S project. Thank you to Sa for teaching me about the $TiSi_2$ system and electrochemical systems. Thank you to all of you that have not been specifically mentioned here for all the help you have provided me.

Thank you to Steve Shepard for all of your help in the clean room, without which I would have been unable to perform my research. Thank you also to Dezhi Wang for

teaching me to use the microscopy instrumentation and for maintaining said equipment, without which I would have been unable to perform my research. I would also like to thank all of the Merkert staff that keep the building running, keep the paychecks coming, and provide us support during our time in the department.

I would like to thank my friends and colleagues at Boston College for their valuable discussions, support, and camaraderie, especially Matt, Grace, and Chris for their regular trips to El Pelón and valuable lunch time chats.

Thank you to my family, my mom especially, for their everlasting support. Without their encouragement and support I would have been unable to make it here and stay in Boston to do what I have done.

To my best friend and love, Miranda, I extend my deepest and most heartfelt gratitude. You have always encouraged me. You have always been there for me. You have always supported me. Thank you.

Chapter 1 : The low-temperature, solid-state conversion of Cu_2S nanowire arrays

1.1 Background

An ever increasing demand for clean energy conversion constantly provides new challenges that can be addressed through materials chemistry. Photovoltaic materials, those that convert electromagnetic radiation to electrical current, can be modified chemically, e.g., by tuning their composition, or mechanically, e.g., by modifying their physical structure. By changing the composition of photovoltaic materials, we can manipulate key parameters that control the performance of photovoltaic devices they compose; these parameters include the band gap and conductivity of the material of interest.[1,2] By modifying the physical structure of a photovoltaic material, e.g., synthesizing the material in the form of NWs or nanorods, the performance of a photovoltaic device can be improved by decoupling the light absorption and charge conduction pathways.[3] As a background to the information contained in sections 1.2–1.7 the proceeding paragraphs in section 1.1 will explain our interest in Cu_2S and how, over time, we arrived at the point of utilizing Cu_2S as a template and chemical precursor to access materials in unique and new morphologies.

In a previous work, Shockley and Quiesser determined the theoretical maximum solar conversion efficiency of a single p-n junction solar cell with a band gap of approximately 1.3 eV to be around 30% (Figure 1.1).[4] A search for a useful photovoltaic material may begin by attempting to find a material with a band gap that would not

limit the efficiency. The aforementioned 1.3 eV band gap factored into our group's decision to study Cu_2S. Cu_2S is an indirect band gap semiconductor with a band gap of approximately 1.2 eV. A promising power conversion efficiency of 17.8% in Cu_2S/ZnO based solar cells has been predicted,[5] and efficiencies of up to 9.15% have been demonstrated in Cu_2S/CdS thin film solar cells.[6] Having selected Cu_2S as a target material, a room-temperature synthesis of Cu_2S NWs was developed in our lab and the growth mechanism was examined.[7] In summary, an ionic vacancy diffusion model was proposed as the growth mechanism: H_2O and S react to form S^{2-}; S^{2-} forms a close-packed sublattice containing vacancies that should contain Cu^+; the Cu^+ vacancies subsequently diffuse to the underlying Cu substrate where they are consumed; and Cu^+ diffuses in the opposite direction to fill the vacancies formed by the S^{2-} sublattice.[7] This high diffusivity of Cu^+ within the sulfur sublattice, demonstrated by the low temperature required for the NW synthesis, would prove to be problematic in our attempts to interface the Cu_2S NWs with CdS to fabricate photovoltaic devices.

In previous works, Cu_xS/CdS solar cells had been demonstrated to degrade through multiple processes, including the diffusion of Cu^+ within the stable sulfur sublattice.[8,9] Although the Cu^+ diffusion proved to be detrimental to the material's implementation in photovoltaic devices, our group found that Cu_2S/ZnO NW devices exhibited negative differential resistance and resistive switching behaviors.[10] An explanation for this behavior was proposed: the high diffusivity of Cu^+ leads to an accumulation of Cu^+ at the Cu_2S/ZnO junction. This accumulation decreases the p-doping of Cu_2S, weakening the

junction between Cu_2S and ZnO and leading to the observed deviations in expected behavior. Although the high diffusivity of Cu^+ led to a discontinuation of its use in photovoltaic materials, our group was able to capitalize upon the behavior to produce devices that could be used for the fabrication of memristors, for instance. This exploitation of the qualities of Cu_2S that were once perceived as negative sets the stage for our utilization of Cu_2S in conversion reactions. That is to say, we are taking an undesired trait of Cu_2S, i.e. the high diffusivity of Cu^+, and utilizing it to obtain other interesting materials.

Our investigation of Cu_2S transformation reactions was prompted by both the high diffusivity of Cu^+ and our failures to successfully fabricate a working Cu_2S/CdS solar cell. Cu_2ZnSnS_4 (CZTS) is an attractive photovoltaic material due to the abundance of Zn and Sn in the Earth's crust. With reported band gaps of 1.45–1.6 eV[11-14] and a theoretical power conversion efficiency of 32.2%[15], CZTS is a worthwhile synthetic target. At the time the conversion research was conducted, there was a lack of reported high-quality CZTS NW arrays. We envisioned a reaction that involved the following process: Cu_2S NW arrays would be coated with a component present in our desired end composition, e.g., Zn; the coated wires would then be exposed to elevated temperatures in a sulfur-rich atmosphere; and after heating, hopefully the coating would be incorporated into the Cu_2S wires through a solid-state diffusion process aided by the diffusivity of the Cu^+. Although we set out to produce vertically-aligned arrays of CZTS NWs, we did not accomplish that goal. However, along the way, we discovered a unique solid-state

reaction process that yielded two interesting structures: an unreported RIT morphology and a segmented NW morphology. The results of our investigations into the conversion of vertically-aligned Cu_2S NW arrays are featured in the remainder of Chapter 1.

The following sections are adapted from the published work: Mayer, M. T.; Simpson, Z. I.; Zhou, S.; Wang, D., Ionic-Diffusion-Driven, Low-Temperature, Solid-State Reactions Observed on Copper Sulfide NWs, *Chem. Mater.,* **2011**, *23* (22), 5045-5051. Copyright 2011 American Chemical Society

1.2 Introduction

With sufficient mixing, applied thermal energy, and time, solid-phase reactants can be transformed into new and possibly interesting materials. The chemical transformation occurs via solid-state diffusion-driven reactions that provide access to tunable binary, ternary, or polynary compositions obtained through a versatile and simple route. By utilizing solid-state reactions, researchers have prepared a plethora of semiconducting, super-conducting, ionic conducting, and magnetic materials.[16] Recent research has highlighted the ability to utilize these reactions to fabricate target materials with specific morphologies, e.g., NWs or nanotubes.[17-20] Although solid-state reactions are versatile and relatively simple, their nature dictates that they proceed at intrinsically slow paces. Due to the slow solid-state diffusion inherent to these reactions, high temperatures, e.g., 500–2000 °C, high pressures, or combinations of the two are usually necessary; these stringent requirements lead to a limitation of both where and

how the synthesis method can be employed. For example, high temperatures were required in works by Gösele et al. that demonstrated the Kirkendall effect formation of hollow structures resulting from heating interfaces between metal oxide heterostructures at temperatures in the range of 500–800 °C.[17,21] Other groups have utilized similar thermally activated solid-state diffusion processes to form unique nanostructures, including Lieber et al.,[22] Wang et al.,[23] Buhro et al.,[24] and others.[25-27] Although these reports utilized nanostructures, which should facilitate a diffusion-controlled reaction due to the small diffusion distances, in each instance, temperatures over 500 °C were required to overcome the significant thermal barrier to diffusion. Other methods have been developed to convert nanostructures; the conversion of nanostructures has been demonstrated using solution-based chemistry at significantly lower temperatures. The use of solution-based approaches is fundamentally different from solid-state reactions, with solvent- or solute-mediated ion exchange being a critical enabling factor in the solution-based reactions.[18,20] As an example, researchers have employed chemical reagents to selectively extract chalcogen anions,[28] or metal cations,[29,30] leaving the nanocrystalline size and shape intact in the converted product. Comparatively, solvent-free, all-solid-state reactions of nanomaterials have been rare.

In this research, solvent-free, solid-state reactions at ambient pressure and at temperatures as low as 105 °C are enabled through the use of Cu_2S as a starting material. Driven by the diffusivity of metal ions in a stable S sublattice, these reactions are shown to yield either unique heteronanostructures, e.g., the RIT structure or

segmented NWs, or fully converted NWs. This mechanism holds promise as a new conversion chemistry for the production of nanostructures with desired morphologies and compositions.

The critical components of this discovery are Cu_2S NWs that grow on Cu, the growth of which follows a recently described cation-vacancy diffusion model.[7] The high diffusivity of Cu^+ within Cu_2S, a hindrance to its utilization in photovoltaic applications[31-33] and a boon to its application in memory storage devices[10,34-36] and solution-phase ion-exchange reactions[29,30] facilitates the aforementioned growth mechanism. In our studies, we further exploited the diffusivity and demonstrated that this unique property can be used to create nanostructures more complex than simple NWs or NRs. By utilizing the Cu_2S NWs as both a template and reactant, we were able to achieve the synthesis of three distinct morphologies, i.e., RIT structures, segmented NWs, and fully converted NWs, at significantly lower temperatures than those normally required for solid-state reactions.[29,30] Interestingly, the reactions were found to exhibit a novel dependence on the basal interface between the NW and the Cu substrate, across which Cu transport takes place.

1.3 Experimental Section

Cu_2S NW Synthesis: Cu_2S NW arrays were synthesized according to a previously published procedure.[7] The synthesis will be briefly outlined here. Cu foils (99.9%, Alfa Aesar) were anodically polished in orthophosphoric acid (85% w/w aq., Alfa Aesar),

rinsed well in water, and dried thoroughly using N_2. The foils were then placed inside a homemade tube reactor and exposed to a gas mixture of N_2, O_2, and H_2S (99.5% chemically pure, Airgas) at flow rates of 160, 80, and 12 sccm, respectively, with the N_2 being diverted through a bubbler filled with water to provide humidity. At room temperature and ambient pressure, a continuous Cu_2S film developed across the Cu substrate, from which vertically aligned Cu_2S NWs emerged over the course of several hours. An extended reaction duration of approximately 36 h can yield NW lengths upward of 5 μm.

Metal deposition: Fe was deposited via sputtering onto as-grown Cu_2S NW arrays using an AJA International ATC Orion sputtering system. Deposition times ranged from 5 to 25 min, resulting in coating thicknesses of approximately 20 nm. The deposition rate was approximately 0.3 $Å\ s^{-1}$ in all instances of Fe deposition. Zn was thermally evaporated onto as-grown Cu_2S NW arrays using a Sharon Vacuum evaporation system. The thicknesses of the Zn coatings were varied between 20 and 120 nm.

Synthesis of Cu–Fe–S Rod-in-Tube Structures: As-deposited Cu_2S/Fe NW arrays were placed in a tube furnace (Lindberg/Blue M model TF55035A-1), purged with N_2 gas (250 sccm), then heated to 105 °C at a rate of 26 °C/min and held at this temperature for 30 min in the presence of N_2 and H_2S at 250 sccm and 12 sccm, respectively. After 30 min had elapsed, the lid of the furnace was opened and the chamber was allowed to cool to room temperature.

Synthesis of Segmented Cu_2S–ZnS and ZnS NWs: The annealing procedure for Zn-coated Cu_2S was similar to that of Fe-coated NWs, except that the Zn incorporation was found to take place with or without the presence of H_2S. In this case, the heating rate was approximately 50 °C min^{-1}, and the final temperature was varied in the range of 105–200 °C. Reaction times were fixed at 30 min.

Structural Characterizations: Micrographs, EDS measurements, and ED patterns were obtained using a JEOL 2010F transmission electron microscope with an electron acceleration voltage of 200 kV, equipped with an Oxford Inca EDS spectrometer.

Statistical Study of Nanostructure Sizes: For the statistical determination of nanostructure diameter change upon heating, at least 100 measurements were performed by TEM observation of two different Cu_2S NW specimens, followed by 100 measurements after heat treatments on metal-coated Cu_2S.

1.4 Fe–Cu_2S System

The RIT morphology is accessed through the heating of Fe-coated Cu_2S NWs in an environment of N_2 and H_2S gases; Figure 1.1 demonstrates the obtained morphology: a rod nested within a tube, each individual part being a discrete structure. This unique morphology was discovered through our attempt to access the Fe–Cu_2S system which was prompted by the potential of pyrite (FeS_2),[37-39] chalcopyrite ($CuFeS_2$),[40] and related materials in electronic, magnetic, and energy-related applications. At the time of publishing and to the best of our knowledge, NWs belonging to the Fe–Cu_2S class of

materials, particularly those in a vertically aligned form, had not been reported previously. This lack of Fe−Cu_2S materials in interesting morphologies may be addressed by using Cu_2S NW arrays as a new precursor and templating platform.

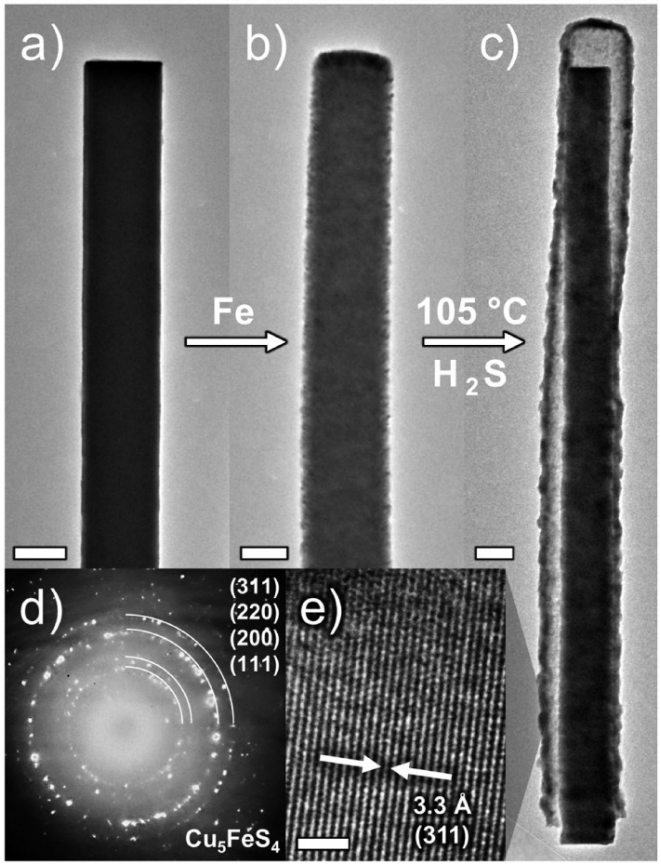

Figure 1.1. An overview of the Cu_2S NWs before and after the conversion process. (a) A TEM micrograph of a Cu_2S NW before an Fe coating was applied. (b) A Cu_2S NW with a 20 nm Fe coating applied via sputtering. (c) The RIT morphology after the Fe-coated Cu_2S NW had reacted at 105 °C in N_2/H_2S for 30 min. The scale bars in 1.1a,b,c represent 100 nm. (d) An electron diffraction pattern of the tube material depicted in 1.1c. The electron diffraction pattern was indexed to the Cu_5FeS_4 bornite phase (JCPDS no. 83-2266). (e) A high resolution TEM micrograph depicting the quality of the crystalline domains in the polycrystalline tube. The scale bar represents 2 nm. Reprinted with permission from *Chem. Mater.*, **2011**, *23* (22), 5045-5051. **Copyright 2011 American Chemical Society.**

As a proof-of-concept, we used sputtered thin films of Fe (approximately 20 nm in thickness) on preformed Cu_2S NWs as the starting material (Figure 2.1a and b). A brief

heating treatment of 30 minutes under a gas flow of 5% H_2S and 95% N_2 (by volume) at 105 °C was sufficient to produce the morphology depicted in Figure 1.1c. In order to determine that the transformation was not limited to only a handful of NWs, over 100 structures were examined; examinations revealed that the rod and tube in each RIT structure are clearly separated by a hollow void, distinguishing the RIT morphology from the more commonly reported core/shell morphologies. Low-magnification TEM images showed that the tubes were continuous from the base, where the NWs were physically connected to the Cu substrate from which they grew, to the encapsulated tip (Figure 1.1c), with tube wall thicknesses varying in the range of 25−50 nm. High-resolution TEM indicated that the tubes were polycrystalline in nature, with grain sizes ranging between 5 and 30 nm (Figure 1.1e, and Figure 1.2). The high-resolution TEM images were consistent with the interpretation of the ED patterns (Figure 1.1d). Elemental analysis of the tube material by EDS revealed the average ternary composition of 54.5% Cu, 12.4% Fe, and 33.1% S, in good agreement with the ED characterizations, whose patterns were indexed to the Cu_5FeS_4 phase (JCPDS no. 83-2266). While the EDS-measured composition deviates from Cu_5FeS_4, several factors may contribute to the observed deviation of stoichiometry. These factors include the inaccuracies of elemental analysis by EDS and the possibility of excess Cu and Fe within a reasonable range (see Figure 1.2 and its caption for further discussion).

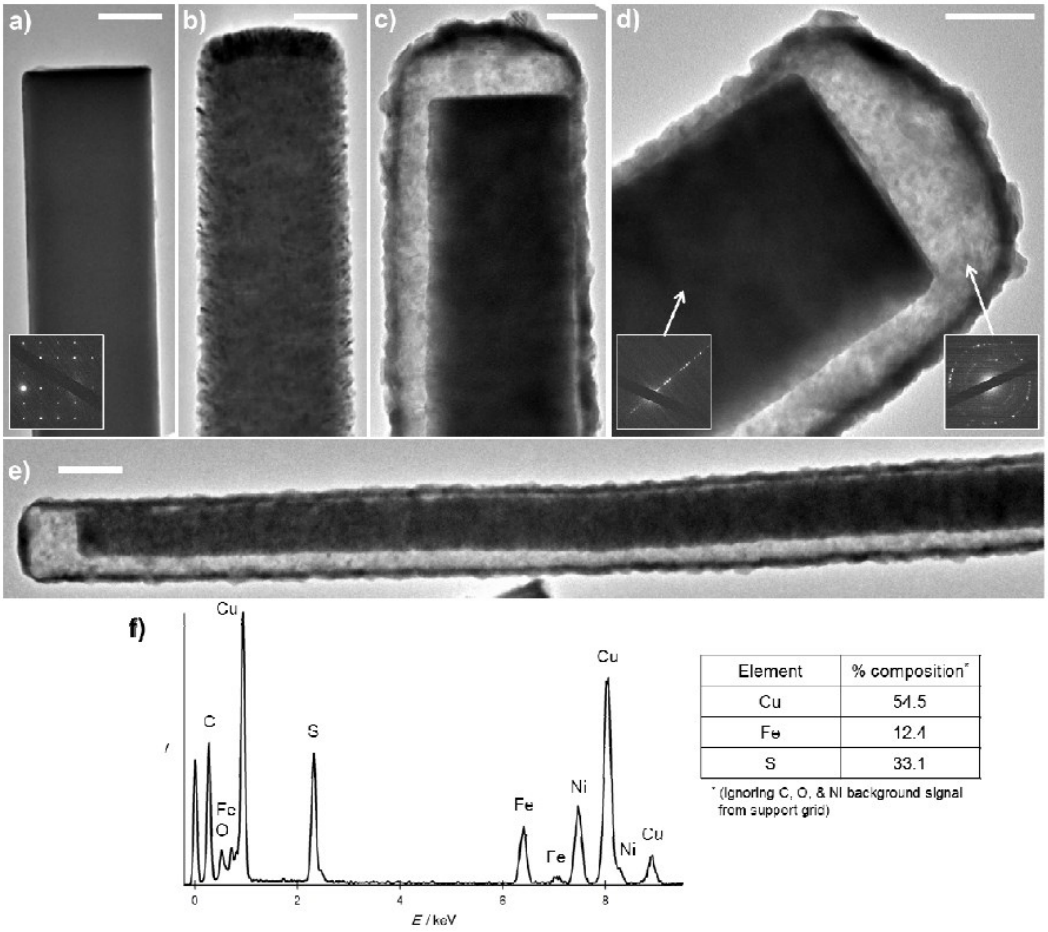

Figure 1.2. Representative TEM micrographs depicting the reactants and products involved in RIT formation reaction. (a) An as-grown, uncoated Cu_2S NW; the scale bar is 100 nm, and the inset is an electron diffraction pattern generated from the Cu_2S NW. (b) A Cu_2S NW that has been coated with approximately 20 nm of Fe utilizing a sputtering method; the scale bar is 100 nm. (c) The RIT morphology that results from heating the Fe-coated Cu_2S NW at 105 °C in 5% H_2S (by volume) for 30 minutes; the scale bar is again 100 nm. (d) A high resolution image of the tip and void space of an individual RIT. The leftmost inset demonstrates the preserved crystallinity of the encapsulated wire and the rightmost inset demonstrates the polycrystalline nature of the Cu_5FeS_4 tube; the scale bar in this image is 100 nm. (e) An overview of the RIT structure; the scale bar is 200 nm. (f) A representative EDS spectrum of the tube and tabulated average percent compositions of the tube material. The observed composition varies from Cu_5FeS_4 with an expected composition of 50% Cu, 10% Fe, and 40% S, and this may be accounted for by the following three reasons: i) 3 $Cu^+ + Fe^0 \rightarrow 3\ Cu^0 + Fe^{3+}$ is spontaneous, based on standard reduction potentials, and may result in metallic Cu being trapped in different portions of the shell; ii) excess unreacted Fe^0 may remain from the deposition; and iii) sulfur may be lost from the porous, high-surface area tube due to vacuum exposure in TEM observation. Reprinted with permission from *Chem. Mater.*, **2011**, *23* (22), 5045-5051. **Copyright 2011 American Chemical Society.**

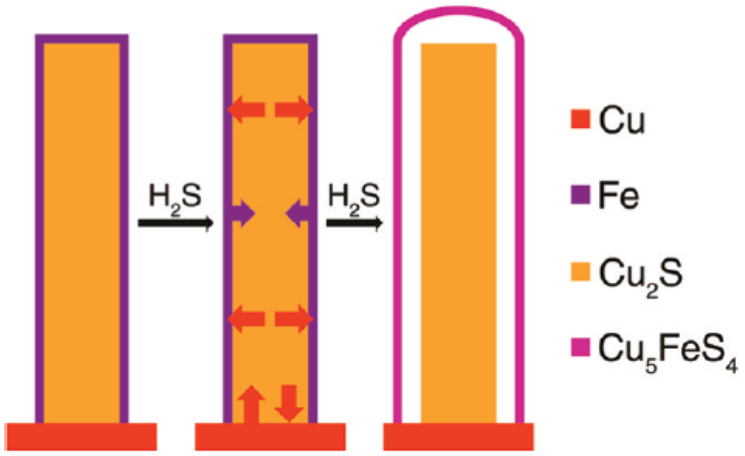

Figure 1.3. A schematic depiction of RIT morphology formation. The magnitudes of the arrows depict the fast Cu diffusion and slow Fe diffusion through the stable S sublattice. Reprinted with permission from *Chem. Mater.*, **2011**, *23* (22), 5045-5051. **Copyright 2011 American Chemical Society.**

We postulate that the reaction proceeds through a mechanism similar to the Kirkendall effect, in which the highly diffusive Cu^{+} ions are critical to the observed transformation. As shown schematically in Figure 1.3, the outward diffusion of Cu^{+} is driven by the formation of ionic vacancies in the shell which result from the sulfidation of Fe, in which H_2S serves as an oxidizer. During subsequent examination after the completion of the reaction, Fe was confirmed to be present in the inner, enclosed rods by EDS examination. This observation suggests that Fe^{2+} ions also diffuse inward, albeit to a lesser extent than the Cu^{+} diffusing outwards. The imbalance between Cu^{+} and Fe^{2+} diffusion results in a significant incorporation of Cu^{+} by the shell. As sulfidation of the shell continues and as vacancies accumulate at the core−shell interface, a separation and expansion of the shell occurs. This separation and expansion lead to the observed

RIT morphology. After physical separation between the rod and the outer tube occurs, the Cu^{+} diffusion routes are likely cut off and any further expansion of the tube results from the continuous supply of sulfur from the gas phase. Literature reports regarding the diffusion rates of Cu and Fe in chalcopyrite $CuFeS_2$ support these observations; in the temperature range of 100−300 °C, the upper limits of the diffusion coefficients for Cu and Fe are 9.4×10^{-7} and 5.4×10^{-12} cm^2/s, respectively.[41] Although this reaction shares similarities with a typical Kirkendall process, it is different because the core NW is not consumed by the process owing to a continuous supply of Cu from the substrate. This hypothesis is supported by the following observations.

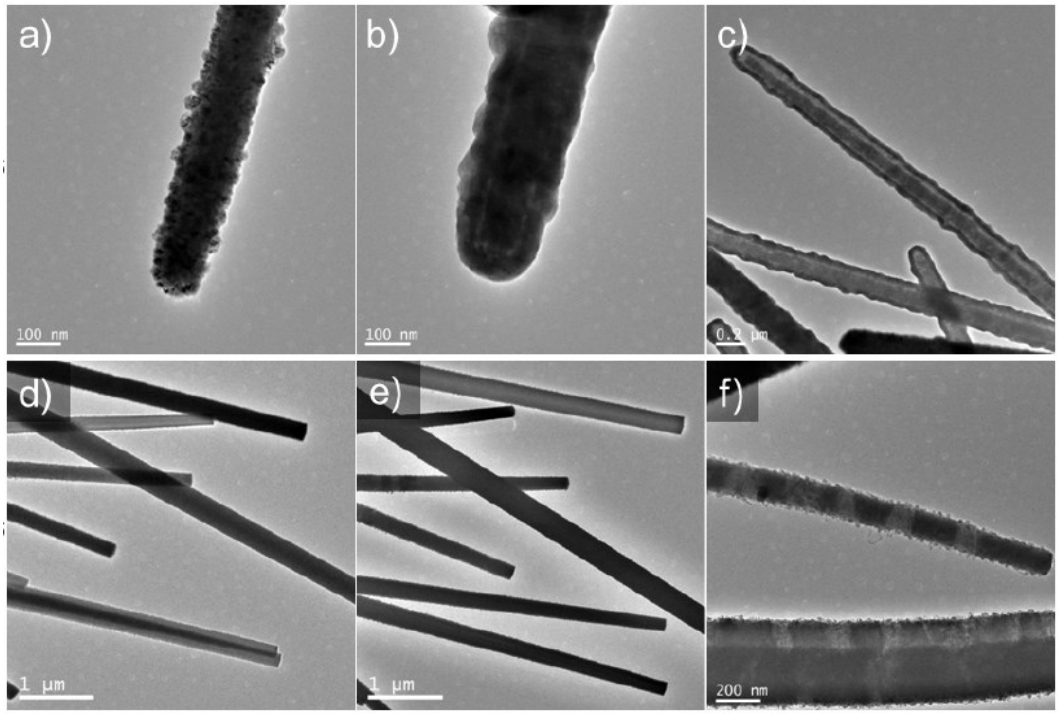

Figure 1.4. TEM micrographs demonstrating the suppression of diffusion-driven reactions caused by the electron beam effect. (a) An Fe-coated Cu_2S NW that has been exposed to an e-beam before the conversion reaction. (b) The same NW after heating the Fe-coated NW to 105 °C in 5% (by volume) H_2S. After reaction, the wire has thickened but does not exhibit the typical expansion into a tube that is demonstrated by unexposed wires. (c) Other NWs in the

same sample that were not exposed to the e-beam before heating; these samples exhibit the typical RIT morphology. (d) Zn-coated Cu_2S NWs at room-temperature. (e) The same wires from panel d after *in situ* heating within the TEM to a temperature of 200 °C. These wires show few signs of Zn incorporation. (f) Other wires in the same sample that were not exposed to the e-beam prior to *in situ* heating reacted normally, exhibited the typical segmented Zn incorporation. Reprinted with permission from *Chem. Mater.*, **2011**, *23* (22), 5045-5051. **Copyright 2011 American Chemical Society.**

First, the RIT morphology was less pronounced or entirely absent when the diffusion of Cu^+ was disrupted. Three avenues were utilized to disrupt the diffusion of Cu^+: electron beam irradiation, disconnection of Cu_2S NWs from the underlying Cu substrate by physical removal, and the use of an intermediate blocking layer of Al_2O_3. Previous studies from our group indicated that the ionic behavior of Cu^+ can be forced to deviate significantly from expected thermodynamically defined behaviors by irradiating a sample with a high energy electron beam which concentrates Cu^+ within the NWs and hence reduces its mobility.[7] Using this knowledge, we designed an experiment in which Fe-coated Cu_2S NWs were exposed to a 200 keV TEM e-beam prior to carrying out the reaction in H_2S; we found that when the NWs had been treated in this manner, the RIT morphology did not form. Interestingly and in contrast to the observed behavior, unexposed NWs in close proximity to electron beam exposed wires reacted normally, yielding the RIT morphology; this behavior is demonstrated in Figure 1.4a-c. These results, in conjunction with our experience with electron beam exposed Cu_2S NWs lead us to conclude that the electron beam irradiation is critical in producing the differences between wires. The disruption of the RIT morphology formation also occurs when Cu_2S NWs are separated from the underlying Cu substrate before heating; the extent of the rod-in-a-tube reaction is less pronounced and a noticeable Cu out diffusion from the

bases of the wires occurs (Figure 1.5a). In this experiment, Cu^+ diffusion is also disrupted, but rather than being caused by electron beam exposure, the cause lies in the removal of the Cu substrate; the Cu substrate acts as a reservoir to receive excess Cu^+ ions or to replace depleted Cu^+ in the Cu_2S NWs, and the removal of this reservoir leads to a disruption in Cu^+ diffusion behavior.[7] In a third experiment in which we attempted to disrupt diffusion between the NWs and their Fe coatings, an intermediate layer of Al_2O_3 was deposited via sputtering between the Cu_2S and Fe coating (Figure 1.6) before carrying out the reaction. The presence of a blocking layer led to a decreased concentration of Cu compared to unblocked reactions and less-pronounced expansion and separation of the shells from their core NWs; a thicker Al_2O_3 coating may have led to an even more drastic reduction in the extent of the reaction. The fact that Cu^+ diffusion is critical to the formation of the RIT structure is reinforced by this third experiment and highlights the important role that the Cu^+ diffusion plays in the formation of this unique morphology.

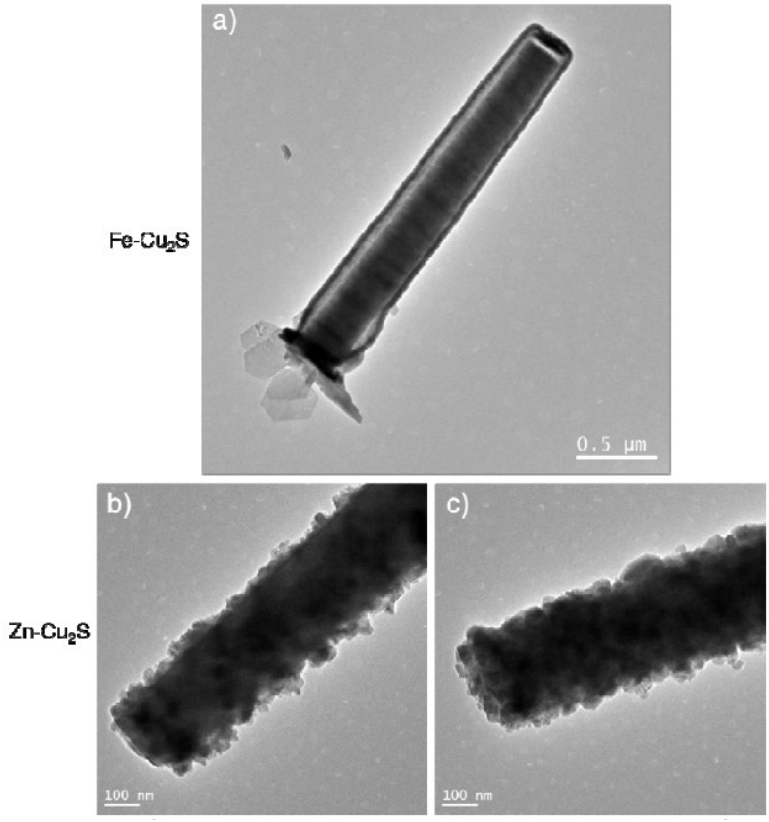

Figure 1.5. Images depicting the results of heating metal-coated Cu_2S NWs after having removed them from the underlying Cu substrate. (a) Fe-coated wires still form the RIT structure, but the expansion is significantly less pronounced and a significant amount of Cu has diffused out from the base of the wire. (b) A Zn-coated Cu_2S NW that has been scraped from its supporting Cu substrate onto a C-film TEM grid. (c) The same wire from panel b after heating the grid under the listed reaction conditions; no noticeable Zn incorporation occurred. Reprinted with permission from *Chem. Mater.*, **2011**, *23* (22), 5045-5051. **Copyright 2011 American Chemical Society.**

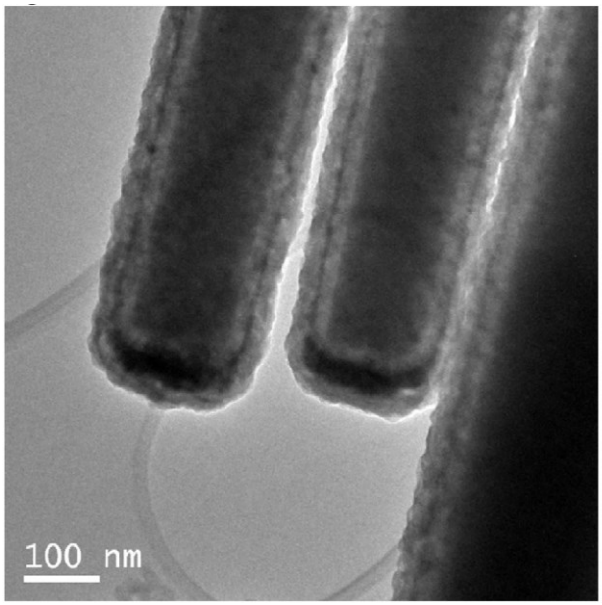

Shell material composition	
Element	% composition
Cu	28.2
Fe	38.2
S	33.6

Figure 1.6. A TEM image demonstrating the effect of a thin Al_2O_3 blocking layer placed between the Cu_2S NWs and the deposited Fe; EDS composition analysis is also tabulated to the right of the picture. The presence of the Al_2O_3 layer led to a small separation of the Fe coatings and the NWs. The significantly inhibited diffusion of Cu^+ is also apparent in the resulting shell composition. Reprinted with permission from *Chem. Mater.*, **2011**, *23* (22), 5045-5051. **Copyright 2011 American Chemical Society.**

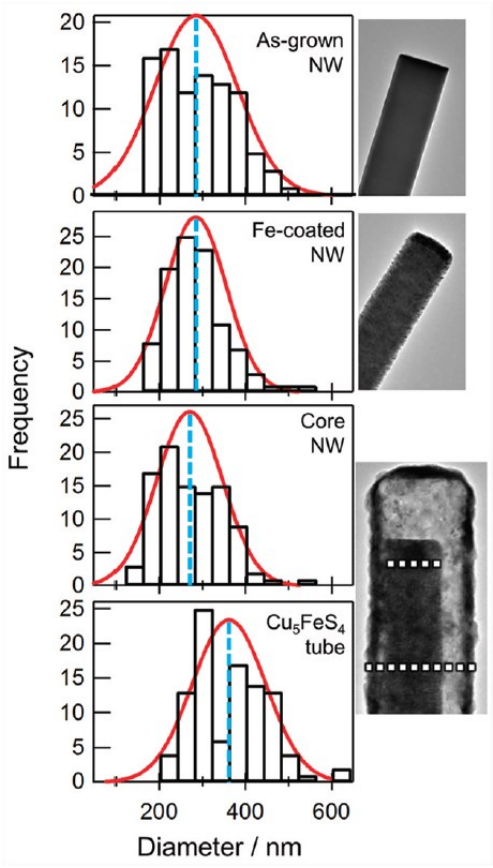

Figure 1.7. In this figure, the statistical measurements of as-grown NWs, Fe-coated NWs, core NWs after reaction, and Cu_5FeS_4 tube, are presented. For each histogram, 100 measurements of the listed structure were collected. A Gaussian fit for each set is presented in red and the average of the set is represented by the dotted blue line. Reprinted with permission from *Chem. Mater.*, **2011**, *23* (22), 5045-5051. **Copyright 2011 American Chemical Society.**

Upon noting that the inner rods in the RIT structure appeared to be unchanged in diameter after reaction, a closer inspection was warranted. Statistical investigations of the diameters of the starting Cu_2S NWs and the resulting rods and tubes were performed; interestingly, the diameters of the encapsulated rods were approximately the same as those of the starting NW templates (Figure 1.7), suggesting that there are no measurable changes in the sublattice of the Cu_2S NWs during reaction. The final stoichiometry of the outer shell suggests that a large amount of Cu^+ moves from the

encapsulated rod to the outer shell before disconnection occurs, and the amount of Fe diffusing inward to the NWs is not nearly enough to replenish the vacancies left by the outward diffusion of Cu^{+}. Since the influx of Fe is not sufficient to maintain electroneutrality, Cu^{+} must be replenished by the only other source from which to draw cations during the reaction: the underlying Cu foil from which the Cu_2S NWs were grown. Lastly, no RIT formation was observed when Fe-coated Si NWs or ZnO NWs were heated under similar conditions (Figure 1.8). From this we infer that the sulfidation of Fe alone is insufficient for the RIT formation. When considering the outcomes of all three experiments, it is clear that a continual supply of Cu from the substrate is critical to the formation of the RIT morphology. This dependence upon a supply of Cu differentiates the structures from the common zero-dimensional analogues referred to as “rattle” or “yolk-shell” nanostructures, or nanotubes formed from core/shell NWs, both of which generally form via a normal Kirkendall process in which the core material is consumed and depleted during the reaction process.[21]

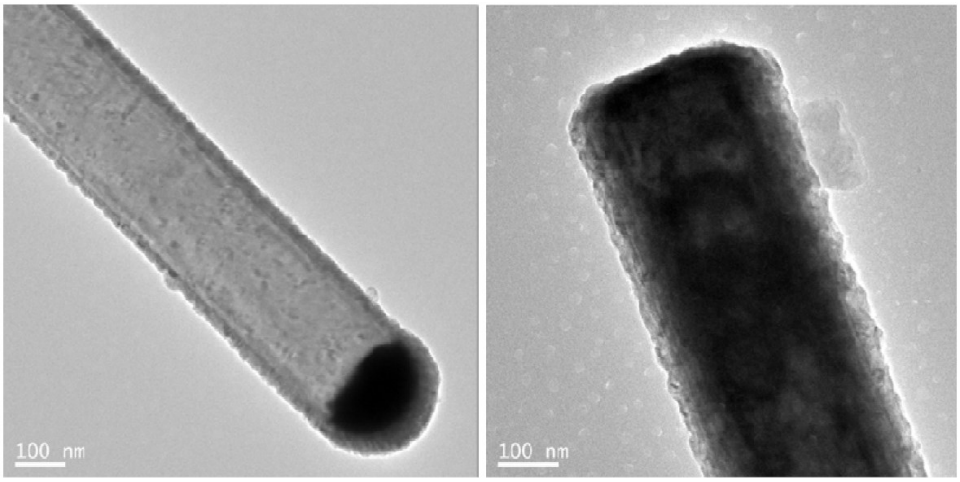

Figure 1.8. TEM micrographs of control experiments involving exposing Fe-coated NWs of compositions other than Cu_2S to the conversion reaction conditions. (a) An Fe-coated Si NW that has been exposed to conversion reaction conditions. The dark spot on the tip of the NW is a Au growth catalyst particle from the VLS NW synthesis. (b) An Fe-coated ZnO NW that has been exposed to the conversion reaction conditions. Neither sample demonstrated significant tube formation or expansion. Reprinted with permission from *Chem. Mater.*, **2011**, *23* (22), 5045-5051. **Copyright 2011 American Chemical Society.**

The temperature at which the RIT morphology forms is highly unusual when compared to other solid-state reactions that result in hollow inorganic structures that derive their morphology from the reaction of a core/shell structure.[21,25,42,43] The high diffusivity of Cu^+ is likely the enabler of the low-temperature reaction. Proceeding at 105 °C, the reaction temperature coincides with the Cu_2S phase transition from monoclinic to hexagonal (i.e., low- to high-chalcocite), with the latter phase known to exhibit increased Cu mobility.[44-46] TEM and ED observations suggest that such a transition may play a role in activating this reaction (Figure 1.2). During our investigations, we also discovered that the role of H_2S in the transformation reaction is a critical one. When Fe-coated Cu_2S NWs were heated at 105 °C in an environment containing no H_2S, no significant morphology or crystal structure changes were observed. Although to fully

understand the role of H_2S, more research would be required; we currently believe it serves at least two purposes: the reaction between H_2S and Fe creates ionic vacancies in the Fe-shell to drive Cu^+ diffusion outward and a continuous reaction between H_2S and the Cu-incorporated Fe-shell leads to further shell expansion and subsequent disconnection from the underlying Cu_2S NWs. Further oxidation of multivalent Fe ions driven by the decomposition of H_2S likely occurs to maintain electroneutrality once the Cu^+ diffusion pathway is broken. Afterward, the shell continues to expand until a thermodynamically stable phase of the Cu−Fe−S system is formed (i.e., bornite).

Although ionic-solubility-effect-driven ionic exchange reactions have been reported at similarly low temperatures,[29,30] reports of low-temperature, solid-state, diffusion-driven reactions in solvent-free systems are rare.[47-49] Thus, our results are deemed to be both significant and new. These results demonstrate the potential of using Cu_2S NWs as both physical templates and chemical precursors to generate high-quality, closed-end, hollow tubes which may be harvested for use in varying applications.

1.5 Zn−Cu_2S System

Although a scenario had been examined in which the outward diffusion of Cu^+ was much greater than the diffusion of another metal ion inward, a situation in which the diffusion of both ions was comparable had yet to be investigated. In order to rectify this situation and to further validate the hypothesis that Cu^+ diffusion enables low-temperature, solid-state reactions, we next examined the Zn-Cu_2S system. Zn was

utilized as the deposited coating on Cu_2S NWs instead of Fe because Zn^{2+} is of similar size to Cu^+ and has been observed to exhibit appreciable diffusivity within a sulfide sublattice.[50-52] Our interest in exploring new synthetic routes to obtain complex chalcogenides for energy conversion applications, such as Cu_2ZnSnS_4 (CZTS),[53,54] the production of which in a vertically aligned NW form remains a challenge,[55] led to our utilization of Zn to access the Zn−Cu_2S system. The resulting morphology was distinctly different from the morphology formed in the Fe−Cu_2S system.

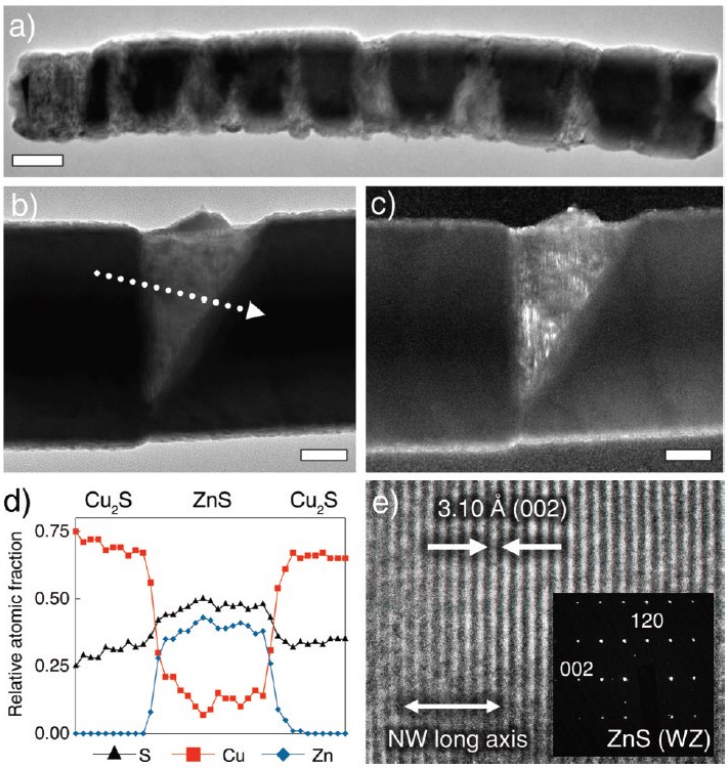

Figure 1.9. The solid-state reaction of Zn-coated Cu_2S NWs. (a) A TEM micrograph featuring the overall segmented incorporation of Zn into a Cu_2S NW; the scale bar is 100 nm. (b) A bright-field image demonstrating the abrupt interface between ZnS and Cu_2S segments; the scale bar is 50 nm. (c) A dark-field image to further highlight the interfaces; the scale bar is 50 nm. (d) The results from an EDS line scan (the scanning path is shown in panel b by the dotted line) that show the Cu_2S and ZnS compositions of the alternating segments. (e) A high-resolution TEM image shows the lattice-resolved spacing that is attributable to the wurtzite ZnS phase; this assignment is corroborated by the inset ED pattern that can be indexed to wurtzite ZnS.

By heating Zn-coated Cu_2S NWs at 105 °C for 30 min in the presence of H_2S, we were able to obtain a segmented NW morphology, as depicted in Figure 1.9. Upon examining the NW samples using bright-field TEM, we found that the dark segments in Figure 1.9a and 1.9b were Cu_2S and the gray segments were ZnS; segment identification was achieved by performing an EDS line scan across the alternating segments, as seen in Figure 1.9d. To determine the crystal structure of the ZnS segments, ED patterns were collected; indexing of the ED patterns led to the conclusion that the ZnS segments are present in the wurtzite phase (Figure 1.9e, inset). The observed interfaces between ZnS and Cu_2S segments were sharp and abrupt, as evidenced by both the TEM images and the EDS line scan. A statistical analysis was carried out on the diameters of the converted NWs; on average, ZnS segment diameters were similar to the Cu_2S NW diameters before conversion and the Cu_2S segment diameters increased markedly (Figure 1.10). From these observations and those that follow, we present the reaction mechanism as we understand it.

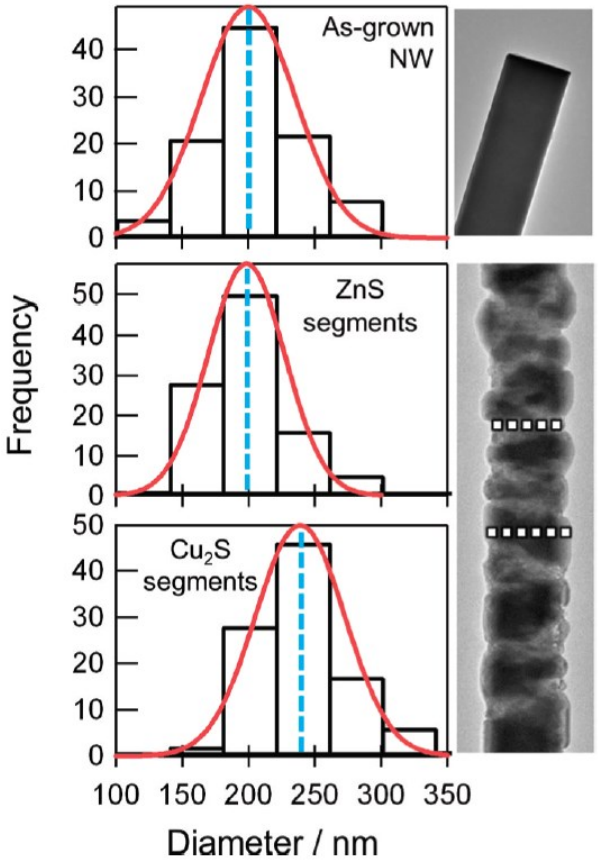

Figure 1.10. Statistical diameter measurements of the Zn-coated Cu_2S NW conversion process. Each histogram comprises 100 diameter measurements of as-grown Cu_2S NWs, ZnS segments after conversion, and Cu_2S segments after conversion. A Gaussian fit is presented in red on each panel and the average is represented by a dotted blue line. Reprinted with permission from *Chem. Mater.*, **2011**, *23* (22), 5045-5051. **Copyright 2011 American Chemical Society.**

Zn^{2+} ions are produced by the oxidation of the deposited Zn coating; these ions are mobile and can diffuse into and throughout the sulfide sublattice to occupy the interstices. As Zn^{2+} diffuses inward, Cu^{+} is displaced and concentrated into adjacent portions of the wire, leading to the formation of the segmented structure that we have observed. This mechanism can be likened to phase segregation in a multicomponent system. The increased diameters of the Cu_2S segments in the final structures can be attributed to further reaction with the H_2S present in the reaction environment. The

proposed mechanism is summarized schematically in Figure 1.11, and we offer the following observations to support our claim.

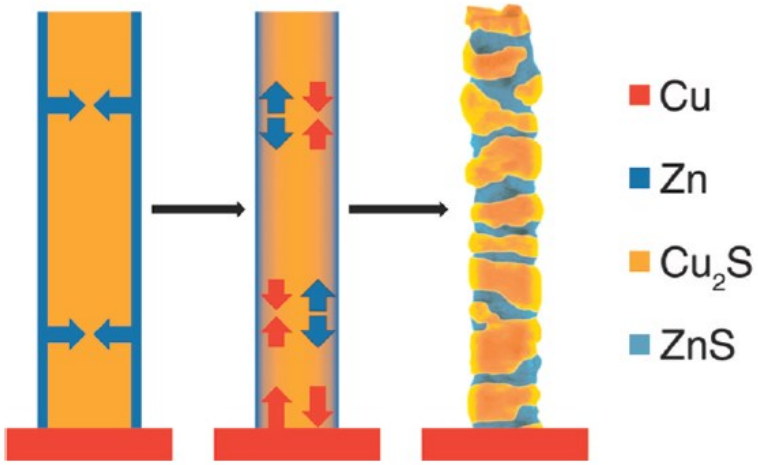

Figure 1.11. Schematic representation depicting the ionic diffusion which drives the formation of segmented ZnS/Cu_2S heterostructured NWs. An inward diffusion of Zn leads to Cu diffusion to either the surface of the NW or back into the Cu substrate. Reprinted with permission from *Chem. Mater.*, **2011**, *23* (22), 5045-5051. **Copyright 2011 American Chemical Society.**

Control experiments that were utilized in the probing of the Fe−Cu_2S system were also utilized to examine the Zn−Cu_2S system. Electron beam irradiation and removal of the underlying Cu substrate (Figure 1.4d-f; Figure 1.5b and c) resulted in significantly less pronounced or no conversion. Although H_2S was critical for the conversion process that occurred in the Fe−Cu_2S system, it was found to play a noncritical role in the Zn−Cu_2S conversion process, a distinguishing difference between the two reactions; it should be noted, however, that the implementation of H_2S in the Zn−Cu_2S conversion process led to smoother surfaces on post-reaction segmented NWs (Figure 1.12). This phenomenon can be explained by the ionic diffusions. Because the reaction with H_2S is not a prerequisite for the Zn^{2+} and Cu^{+} diffusion, the segregation takes place with or without

H_2S. When H_2S is absent, the excess Cu concentrates on the surface of the Cu-rich segments to yield rough morphologies. When H_2S is present, the dynamic reactions between Cu and H_2S result in smooth surfaces and increased diameters of the Cu-rich segments. That H_2S is not critical for the reactions with Zn further suggests that Zn can be oxidized by Cu^+. The reaction $Zn + Cu_2S \rightarrow Cu + ZnS$ is exothermic ($\Delta_r H° = -126.5$ kJ mol^{-1}), reinforcing the fact that H_2S plays a non-critical role and that Zn can be oxidized by the Cu^+ found within the Cu_2S NWs.

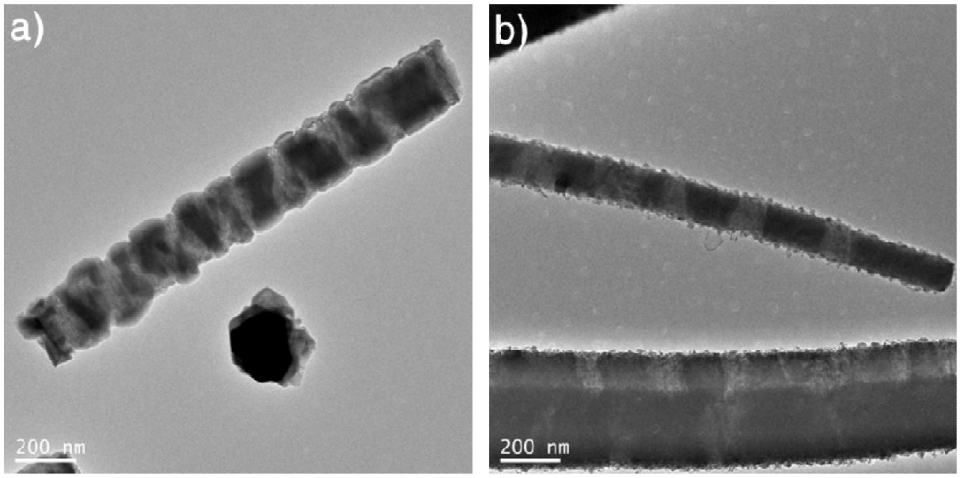

Figure 1.12. Segmented NWs form from heated Zn-coated Cu_2S with or without the presence of H_2S. (a) When H_2S is used in the conversion reaction, the dark Cu_2S segments are smooth and bulging. (b) NWs that are converted through *in situ* heating in a TEM column result in surfaces that are less smooth. Reprinted with permission from *Chem. Mater.*, **2011**, *23* (22), 5045-5051. **Copyright 2011 American Chemical Society.**

There did not appear to be a specific pattern or order to the arrangement of the segments formed after the conversion of the NWs occurred. We also found that the amount of Zn incorporated into the underlying Cu_2S NWs was dependent upon the amount of Zn deposited before the reaction occurred. Because the supply of Zn is the limiting factor in the conversion reaction, we postulate that the segmented NWs that

were initially observed reflect a partial conversion; to test whether this was the case, the thickness of the Zn coating was increased to roughly 90 nm before carrying out the conversion reaction. After the reaction, we found that the initial Zn-coated Cu_2S NWs had been converted to ZnS NWs. The converted ZnS NWs are displayed in Figure 1.13 in both bright- and dark-field TEM images. Trace amounts of Cu were noted to be present when examining the wires with EDS. However, the remaining Cu is likely present in the form of Cu_2S or Cu embedded within the wire or on the surface. Although Cu was present after conversion, the amount does not account for the original Cu content present in the Cu_2S template. Since the amount of Cu retained after full conversion is limited, the excess Cu^+ must be displaced into another location; the only location to which the excess Cu^+ can be moved is to the underlying Cu support. The possibility of such displacement is quite possible when considering the fact that the Cu_2S NWs are attached to a reservoir for the outward diffusing ions: the Cu substrate. The dark-field image appears to show strain within the NW lattice, presumably due to the lattice mismatch between ZnS and Cu_2S. The amorphous particles on the surface are primarily excess Zn.

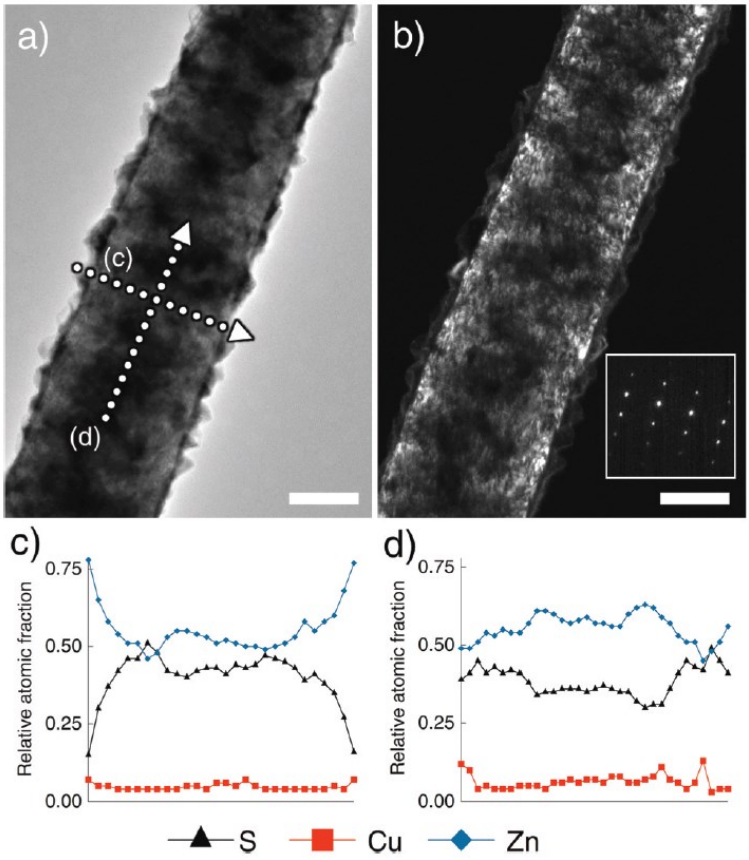

Figure 1.13. Full conversion from Cu_2S to ZnS NWs. (a) A bright-field TEM image depicts the texture of excess Zn on the NW surface. (b) A dark-field TEM image depicts the intact crystallinity of the NW; the crystallinity is corroborated by the inset ED pattern that can be indexed to wurtzite ZnS. The scale bars of both panels a and b are 100 nm. (c) Radial and (d) axial EDS line scans verify the lack of Cu and the presence of ZnS and excess Zn. Reprinted with permission from *Chem. Mater.*, **2011**, *23* (22), 5045-5051. **Copyright 2011 American Chemical Society.**

Distinctly different morphologies were obtained through the utilization of the Zn−Cu_2S reaction, morphologies which were strikingly different from the RIT structures produced by the Fe−Cu_2S system, demonstrating the versatility of the solid-state process. The resulting segmented NWs suggest a simple reaction process for achieving compositionally modulated NWs which may be shown to demonstrate unique opto- or thermo-electronic properties. Finally, the full conversion from Cu_2S to ZnS NWs may

offer a method for achieving, through conversion reactions, other NWs of varying target compositions.

1.6 Materials Considerations

Appreciable ion diffusion at low temperatures and an interface between Cu_2S and the Cu substrate across which mass transfer occurs are two key characteristics of the Cu_2S NW arrays that enable the aforementioned conversion reactions. Although the conversion reactions in this section were demonstrated using Cu_2S—a material well-known for its highly diffusive Cu cations—as a precursor material, there is no reason to discount the possibility that this approach may be extended to other chemical systems, even some that are not known for their high ionic diffusivities, which may behave in a similar fashion when utilized in solid-state reactions. The large variety of compounds in which solution-based low-temperature exchange reactivity have been demonstrated, including a large number of metal chalcogenides and oxides, supports the notion that the conversion reaction presented in this text may be extensible to other systems.[18,20,29,30,56,57] In a manner that is similar to the results of the previously mentioned studies, the nanoscale effect of increased reactivity may permit solid-state reactions in such materials via similar mechanisms to those presented herein.

1.7 Conclusions

A defining attribute of the Cu_2S system that renders it to be unique is the diffusivity of Cu^+ within the S sublattice. An equally unique characteristic found within the Cu_2S

system is the presence of ionic diffusion channels between the NWs and the substrate from which the NWs grow; These ionic diffusion channels can be utilized to provide additional Cu^+ or to store excess Cu^+ as evidenced in the Fe−Cu_2S and Zn−Cu_2S systems, respectively. A more interesting result of the combination of differing diffusion rates, a high Cu^+ diffusivity, and a reservoir to provide and collect Cu^+ is the production of two very different morphologies, one of which, the RIT morphology, has been observed for the first time. While this current research did not explore applications for the resultant structures, they may prove to be useful in various applications; for example, the increased surface of area and available void space of the RIT structure may be suitable for catalysis or sensing applications, and the segmented wires may prove to possess interesting thermoelectric and optoelectronic properties. Moreover, the reactive template, Cu_2S, may be further exploited to obtain more complex conversion reactions, e.g., the production of Cu_2ZnSnS_4, with the target materials being attractive solar energy harvesting candidates.

1.8 References

1. Vurgaftman, I.; Meyer, J. R.; Ram-Mohan, L. R., Band parameters for III–V compound semiconductors and their alloys. *J. Appl. Phys.* **2001**, *89*, 5815-5875.
2. Bertoni, M. I.; Mason, T. O.; Medvedeva, J. E.; Freeman, A. J.; Poeppelmeier, K. R.; Delley, B., Tunable conductivity and conduction mechanism in an ultraviolet light activated electronic conductor. *J. Appl. Phys.* **2005**, *97*, 103713-6.
3. Law, M.; Goldberger, J.; Yang, P. D., Semiconductor nanowires and nanotubes. *Annu. Rev. Mater. Res.* **2004**, *34*, 83-122.
4. Shockley, W.; Queisser, H. J., Detailed balance limit of efficiency of p-n junction solar cells. *J. Appl. Phys.* **1961**, *32*, 510-520.
5. Burgelman, M.; Pauwels, H. J., Theoretical advantages of p-n+-type Cu_2S-ZnO solar-cell. *Electron. Lett.* **1981**, *17*, 224-226.

6. Bragagnolo, J. A.; Barnett, A. M.; Phillips, J. E.; Hall, R. B.; Rothwarf, A.; Meakin, J. D., The design and fabrication of thin-film CdS-Cu_2S cells of 9.15-percent conversion efficiency. *IEEE Trans. Electron Devices* **1980**, *27*, 645-651.
7. Liu, X.; Mayer, M. T.; Wang, D., Understanding ionic vacancy diffusion growth of cuprous sulfide nanowires. *Angew. Chem., Int. Ed. Engl.* **2010**, *49*, 3165-3168.
8. Partain, L. D.; McLeod, P. S.; Duisman, J. A.; Peterson, T. M.; Sawyer, D. E.; Dean, C. S., Degradation of a Cu_2S/CdS solar-cell in hot, moist air and recovery in hydrogen and air. *J. Appl. Phys.* **1983**, *54*, 6708-6720.
9. Cassaignon, S.; Pauporte, T.; Guillemoles, J. F.; Vedel, J., Copper diffusion in copper sulfide: a systematic study. *Ionics* **1998**, *4*, 364-371.
10. Liu, X.; Mayer, M. T.; Wang, D., Negative differential resistance and resistive switching behaviors in Cu_2S NW devices. *Appl. Phys. Lett.* **2010**, *96*, 223103-3.
11. Katagiri, H.; Saitoh, K.; Washio, T.; Shinohara, H.; Kurumadani, T.; Miyajima, S., Development of thin film solar cell based on Cu_2ZnSnS_4 thin films. *Sol. Energy Mater. Sol. Cells* **2001**, *65*, 141-148.
12. Jimbo, K.; Kimura, R.; Kamimura, T.; Yamada, S.; Maw, W. S.; Araki, H.; Oishi, K.; Katagiri, H., Cu_2ZnSnS_4-type thin film solar cells using abundant materials. *Thin Solid Films* **2007**, *515*, 5997-5999.
13. Katagiri, H., Cu_2ZnSnS_4 thin film solar cells. *Thin Solid Films* **2005**, *480–481*, 426-432.
14. Riha, S. C.; Parkinson, B. A.; Prieto, A. L., Solution-based synthesis and characterization of Cu_2ZnSnS_4 nanocrystals. *J. Am. Chem. Soc.* **2009**, *131*, 12054-12055.
15. Guo, Q.; Hillhouse, H. W.; Agrawal, R., Synthesis of Cu_2ZnSnS_4 nanocrystal ink and its use for solar cells. *J. Am. Chem. Soc.* **2009**, *131*, 11672-11673.
16. West, A. R., *Solid State Chemistry and Its Applications*. **1987**.
17. Jin fan, H.; Knez, M.; Scholz, R.; Nielsch, K.; Pippel, E.; Hesse, D.; Zacharias, M.; Gosele, U., Monocrystalline spinel nanotube fabrication based on the Kirkendall effect. *Nat. Mater.* **2006**, *5*, 627-631.
18. Vasquez, Y.; Henkes, A. E.; Chris Bauer, J.; Schaak, R. E., Nanocrystal conversion chemistry: A unified and materials-general strategy for the template-based synthesis of nanocrystalline solids. *J. Solid State Chem.* **2008**, *181*, 1509-1523.
19. Baodan, L.; Yoshio, B.; Xin, J.; Chun, L.; Xiaosheng, F.; Haibo, Z.; Takeshi, T.; Chengchun, T.; Masanori, M.; Dmitri, G., Self-assembled ZnS NW arrays: synthesis, in situ Cu doping and field emission. *Nanotechnology* **2010**, *21*, 375601.
20. Moon, G. D.; Ko, S.; Min, Y.; Zeng, J.; Xia, Y.; Jeong, U., Chemical transformations of nanostructured materials. *Nano Today* **2011**, *6*, 186-203.
21. Fan, H. J.; Gösele, U.; Zacharias, M., Formation of nanotubes and hollow nanoparticles based on Kirkendall and diffusion processes: a review. *Small* **2007**, *3*, 1660-1671.
22. Wu, Y.; Xiang, J.; Yang, C.; Lu, W.; Lieber, C. M., Single-crystal metallic nanowires and metal/semiconductor nanowire heterostructures. *Nature* **2004**, *430*, 61-65.
23. Zhou, J.; Liu, J.; Wang, X.; Song, J.; Tummala, R.; Xu, N. S.; Wang, Z. L., Vertically aligned Zn_2SiO_4 nanotube/ZnO nanowire heterojunction arrays. *Small* **2007**, *3*, 622-626.
24. Trentler, T. J.; Iyer, R. S.; Sastry, S. M. L.; Buhro, W. E., Preparation of nanocrystalline molybdenum disilicide ($MoSi_2$) by a chlorine-transfer reaction. *Chem. Mater.* **2001**, *13*, 3962-3968.

25. Raidongia, K.; Rao, C. N. R., Study of the transformations of elemental nanowires to nanotubes of metal oxides and chalcogenides through the Kirkendall effect. *J. Phys. Chem. C* **2008**, *112*, 13366-13371.
26. Fan, H.-M.; Yi, J.-B.; Yang, Y.; Kho, K.-W.; Tan, H.-R.; Shen, Z.-X.; Ding, J.; Sun, X.-W.; Olivo, M. C.; Feng, Y.-P., Single-crystalline MFe_2O_4 nanotubes/nanorings synthesized by thermal transformation process for biological applications. *ACS Nano* **2009**, *3*, 2798-2808.
27. Li, Y. J.; Lu, M. Y.; Wang, C. W.; Li, K. M.; Chen, L. J., $ZnGa_2O_4$ nanotubes with sharp cathodoluminescence peak. *Appl. Phys. Lett.* **2006**, *88*, 143102-3.
28. Sines, I. T.; Schaak, R. E., Phase-selective chemical extraction of selenium and sulfur from nanoscale metal chalcogenides: a general strategy for synthesis, purification, and phase targeting. *J. Am. Chem. Soc.* **2010**, *133*, 1294-1297.
29. Luther, J. M.; Zheng, H.; Sadtler, B.; Alivisatos, A. P., Synthesis of PbS nanorods and other ionic nanocrystals of complex morphology by sequential cation exchange reactions. *J. Am. Chem. Soc.* **2009**, *131*, 16851-16857.
30. Sadtler, B.; Demchenko, D. O.; Zheng, H.; Hughes, S. M.; Merkle, M. G.; Dahmen, U.; Wang, L.-W.; Alivisatos, A. P., Selective facet reactivity during cation exchange in cadmium sulfide nanorods. *J. Am. Chem. Soc.* **2009**, *131*, 5285-5293.
31. Moitra, K.; Deb, S., Degradation of the performance of Cu_2S/CdS solar cells due to a two-way solid state diffusion process. *Solar Cells* **1983**, *9*, 215-228.
32. Cassaignon, S.; Pauporté, T.; Guillemoles, J. F.; Vedel, J., Copper diffusion in copper sulfide: a systematic study. *Ionics* **1998**, *4*, 364-371.
33. Larson, R. S., A physical and mathematical model for the atmospheric sulfidation of copper by hydrogen sulfide. *J. Electrochem. Soc.* **2002**, *149*, B40-B46.
34. Sakamoto, T.; Sunamura, H.; Kawaura, H.; Hasegawa, T.; Nakayama, T.; Aono, M., Nanometer-scale switches using copper sulfide. *Appl. Phys. Lett.* **2003**, *82*, 3032-3034.
35. Tsuchiya, T.; Oyama, Y.; Miyoshi, S.; Yamaguchi, S., Nonstoichiometry-induced carrier modification in gapless type atomic switch device Using Cu_2S mixed conductor. *Applied Physics Express* **2009**, *2*, 055002.
36. Riha, S. C.; Johnson, D. C.; Prieto, A. L., Cu_2Se nanoparticles with tunable electronic properties due to a controlled solid-state phase transition driven by copper oxidation and cationic conduction. *J. Am. Chem. Soc.* **2010**, *133*, 1383-1390.
37. Wadia, C.; Wu, Y.; Gul, S.; Volkman, S. K.; Guo, J.; Alivisatos, A. P., Surfactant-assisted hydrothermal synthesis of single phase pyrite FeS_2 nanocrystals. *Chem. Mater.* **2009**, *21*, 2568-2570.
38. Puthussery, J.; Seefeld, S.; Berry, N.; Gibbs, M.; Law, M., Colloidal iron pyrite (FeS_2) nanocrystal inks for thin-film photovoltaics. *J. Am. Chem. Soc.* **2010**, *133*, 716-719.
39. Lin, C. W.; Wang, D. Y.; Wang, Y. T.; Chen, C. C.; Yang, Y. J.; Chen, Y. F., Increased photocurrent in bulk-heterojunction solar cells mediated by FeS_2 nanocrystals. *Sol. Energy Mater. Sol. Cells* **2011**, *95*, 1107-1110.
40. Barkat, L.; Hamdadou, N.; Morsli, M.; Khelil, A.; Bernède, J. C., Growth and characterization of CuFeS2 thin films. *J. Cryst. Growth* **2006**, *297*, 426-431.
41. Chen, J. H.; Harvey, W. W., Cation self-diffusion in chalcopyrite and pyrite. *Metal. Trans. B* **1975**, *6*, 331-339.
42. Li, Q.; Penner, R. M., Photoconductive cadmium sulfide hemicylindrical shell nanowire ensembles. *Nano Lett.* **2005**, *5*, 1720-1725.

43. Lee, Y.-I.; Goo, Y.-S.; Chang, C.-H.; Lee, K.-J.; Myung, N. V.; Choa, Y.-H., Tunable synthesis of cuprous and cupric oxide nanotubes from electrodeposited copper nanowires. *J. Nanosci. Nanotechnol.* **2011**, *11*, 1455-1458.
44. Hirahara, E., The electrical conductivity and isothermal hall effect in cuprous sulfide, semi-conductor. *J. Phys. Soc. Jpn.***1951**, *6*, 428.
45. Evans, H. T., Copper Coordination in low chalcocite and djurleite and other copper-rich sulfides. *Am. Mineral.* **1981**, *66*, 807-818.
46. Leon, M.; Terao, N.; Rueda, F., Phase transitions in cuprous sulphide evaporated thin films. *J. Mater. Sci.* **1984**, *19*, 113-120.
47. Wang, Q.; Li, J.-X.; Li, G.-D.; Cao, X.-J.; Wang, K.-J.; Chen, J.-S., Formation of CuS nanotube arrays from CuCl nanorods through a gas-solid reaction route. *J. Cryst. Growth* **2007**, *299*, 386-392.
48. Zhang, B.; Jung, Y.; Chung, H.-S.; Vugt, L. V.; Agarwal, R., Nanowire transformation by size-dependent cation exchange reactions. *Nano Lett.* **2009**, *10*, 149-155.
49. Mokari, T.; Aharoni, A.; Popov, I.; Banin, U., Diffusion of gold into InAs nanocrystals. *Angew. Chem., Int. Ed. Engl.* **2006**, *45*, 8001-8005.
50. Burton, L. C.; Uppal, P. N.; Dwight, D. W., Cross diffusion of Cd and Zn in Cu_2S formed on $Zn_xCd_{1-x}S$ thin films. *J. Appl. Phys.* **1982**, *53*, 1538-1542.
51. Cherniak, D. J., Diffusion in carbonates, fluorite, sulfide minerals, and diamond. *Rev. Mineral. Geochem.* **2010**, *72*, 871-897.
52. Sun, H.; Chen, Y.; Wang, X.; Xie, Y.; Li, W.; Zhang, X., Synthesis of ZnS hollow nanoneedles via the nanoscale Kirkendall effect. *J. Nanopart. Res.* **2011**, *13*, 97-103.
53. Katagiri, H.; Jimbo, K.; Maw, W. S.; Oishi, K.; Yamazaki, M.; Araki, H.; Takeuchi, A., Development of CZTS-based thin film solar cells. *Thin Solid Films* **2009**, *517*, 2455-2460.
54. Todorov, T. K.; Reuter, K. B.; Mitzi, D. B., High-efficiency solar cell with Earth-abundant liquid-processed absorber. *Adv. Mater.* **2010**, *22*, E156-E159.
55. Chan, C. P.; Lam, H.; Leung, K. K.; Surya, C., Growth of copper zinc tin sulfide nano-rods by electrodeposition using anodized aluminum as the growth mask. *J. Nonlinear Opt. Phys.* **2009**, *18*, 599-603.
56. Camargo, P. H. C.; Lee, Y. H.; Jeong, U.; Zou, Z.; Xia, Y., Cation exchange: a simple and versatile route to inorganic colloidal spheres with the same size but different compositions and properties. *Langmuir* **2007**, *23*, 2985-2992.
57. Jeong, U.; Camargo, P. H. C.; Lee, Y. H.; Xia, Y., Chemical transformation: a powerful route to metal chalcogenide nanowires. *J. Mater. Chem.* **2006**, *16*, 3893-389

Chapter 2 : The oxide-stabilization and utilization of $TiSi_2$ nanonets as a lithium-ion battery anode

2.1 Background

An ever increasing demand for portable energy storage continually pressures material scientists to improve existing battery technologies and possibly develop new electrode chemistries. As demand for mobile energy storage increases, challenges pertaining to energy storage are made apparent. Stability, a large capacity, and the ability to charge and discharge a battery quickly are all desirable properties of electrochemical energy storage devices. A brief and non-comprehensive outline of previous anode developments that attempted to meet some of these challenges is provided in the following paragraphs.

Li-ion batteries are composed of multiple electrochemical cells arranged in parallel and/or series to provide target voltages and desired capacities. The individual electrochemical cells comprise an anode and a cathode separated by an electrolyte solution containing dissociated lithium salts that enable Li^+ transport between the anode and cathode. Initial lithium-ion primary batteries, i.e., non-rechargeable, contained a Li metal anode. One of the main shortcomings of the Li metal anode was an uneven deposition of Li during subsequent charging and discharging cycles leading to dendritic growth of Li; the dendrites eventually bridge the two electrodes causing electrical short circuits that could lead to fires or explosions.[1]

To address the issue of dendritic growth that could potentially lead to catastrophic failure of a Li-ion cell, new anode chemistries were investigated. The replacement of a lithium metal anode with an Al-Li alloy addressed the problematic formation of dendrites.[2] Although the shorting issue was addressed through the implementation of Li alloys, they also brought their own challenges. Silicon-based anodes offer high theoretical capacities (4,200 mAh $g^{-}1$) and low discharge potentials.[3,4] Although this material demonstrates attractive characteristics, it also possesses the same problem that plagued earlier alloying electrodes—severe capacity fade occurs due to extreme volume changes caused by the alloying and dealloying of lithium. These volume changes pulverize the electrode. In the case of silicon, the capacity change upon lithiation or delithiation can be as large as 400%.[3]

Lithium-ion cathodes, on the other hand, have been fabricated using layered-type structures rather than lithium alloys. One of the earliest examples of a promising Li-ion battery was Exxon's configuration of a TiS_2 cathode, Li metal anode, and lithium perchlorate in dioxolane electrolyte.[5] Further progress was made in the field of cathode development by moving away from heavier sulfur-containing compounds to lighter oxide materials, which possessed both higher voltages and capacities. In 1980, Mizushima et al. demonstrated that Li_xCoO_2 could be utilized as a Li-ion cathode material.[6] Indeed, the commercial success of Li_xCoO_2 electrodes speaks of their stability and satisfactory performance.

So, what if we could combine the stability imparted through a layered structure with the capacity of a Li alloy while addressing the volume expansion and degradation properties of Li alloy anodes? We would end up with the $TiSi_2$ nanonet, a unique morphology that was previously synthesized in our lab[7] and a promising candidate that possesses the best characteristics of layered- and alloy-type lithium-ion electrodes. $TiSi_2$ NNs have previously demonstrated their versatility as supporting electrodes that can be modified with other functional materials in photoelectrochemical water splitting applications[8] and in both anode[9,10] and cathode[11] roles in Li-ion batteries. Our findings will be covered in the following sections. But briefly, $TiSi_2$ NNs are one of the first reported layered-type structure inorganic anode materials; possess a good specific capacity of approximately 800 mAh g^{-1}; and demonstrate good stability when cycled, losing less than 20% of their original capacity after 500 cycles.

The following sections are adapted from the published work: Zhou, S.; Simpson, Z. I.; Yang, X.; Wang, D., Layered Titanium Disilicide Stabilized by Oxide Coating for Highly Reversible Lithium Insertion and Extraction, *ACS Nano*, **2012**, *6* (9), 8114-8119. Copyright 2012 American Chemical Society.

2.2 Introduction

The lithium-ion battery, a technology that presents significant advantages—such as long cycle lifetimes and comparatively high specific capacities—over competing battery technologies, is currently at the forefront of energy storage technology. Numerous

developments have led to its current position in the energy storage hierarchy, including but not limited to the formulation and discovery of new electrode materials, e.g., graphite anodes and $LiCoO_2$ cathodes. [12] A defining feature of potential electrode materials is that they often possess a layered structure, allowing Li^+ insertion and extraction with minimal negative effects upon the host material's structure; the non-invasive nature of the Li^+ insertion and extraction enables long cycle lifetimes in these layered materials. [1] Although these materials possess a beneficial layered configuration, they also present low measured specific capacities, limited by their chemical nature[13]; with an ever-increasing demand for larger amounts of portable energy storage, layered materials have begun to fall behind. On the other hand, a host of non-layered materials are available for utilization as electrode materials, such as Si,[4,14-16] Si-alloys,[17-19] Sn,[20,21] and SnO_2,[22,23]. While the aforementioned materials possess much higher capacities than their layered counterparts, they also suffer from short cycle lifetimes due to structural degradations caused by the insertion and extraction of Li^+. To push the limits of lithium-ion technology, new layered materials with both high specific capacities and increased cycle lifetimes must be sought. In our work, we found that $TiSi_2$, in a specific, nanostructured configuration, enables the obtainment of the goals of both a high specific capacity and long cycle lifetime; these qualities are conferred by the high Si content found in $TiSi_2$ and the material's layered crystal structure.

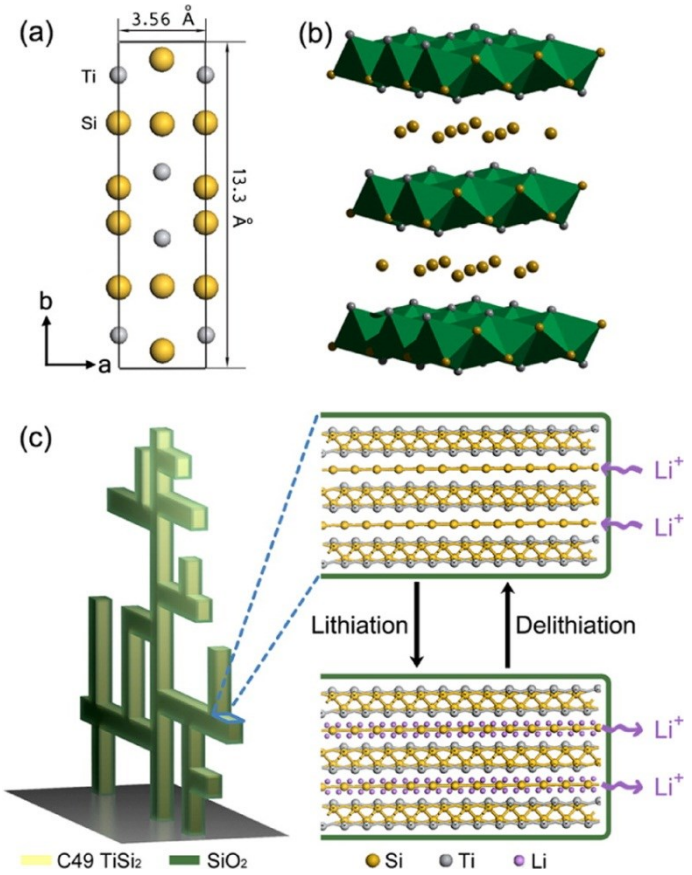

Figure 2.1. The C49 $TiSi_2$ crystal structure—illustrated schematically. (a) A side view of the unit cell when viewed along the [001] direction. (b) A polyhedral representation of the $TiSi_2$ crystal structure. The green polyhedrons are formed by the Ti-Si layer, and the Si-only layers are represented by the intermediate discrete atoms. (c) An overview of the $TiSi_2$ NN structure is displayed on the left. The diagrams on the right depict the Li^+ insertion and extraction process. The outer green boundary represents the oxide coating. Reprinted with permission from *ACS Nano.*, **2012**, *6* (9), 8114-8119. **Copyright 2012 American Chemical Society.**

The $TiSi_2$ NN is unique due to its C49 crystal structure. As shown in Figure 2.1, the structure of $TiSi_2$ comprises flat Si-only layers separated by polyhedrons constructed from Ti and Si. Since Si is well-known for its ability to alloy with Li, it does not take a leap of faith to suspect that the layered C49 structure can serve as an anode material in a Li-ion battery. However, it has been difficult to study this hypothesis because bulk C49 $TiSi_2$ has been reported to be metastable, converting to a C54 structure upon heating.[24]

The latter structure is still of orthorhombic symmetry but lacks the Si-only layers. Without the presence of Si-only layers in C54, the likelihood that Li^+ would be incorporated to a large extent is lessened; accordingly, C54 $TiSi_2$ has been previously demonstrated to not have an appreciable capacity in the Li-ion system.[25] From previous work in our laboratory, it was discovered that the NN form of C49 $TiSi_2$ is stable up to 900 °C, avoiding the unwanted conversion to the low capacity C54 structure.[7] Although we have not undertaken in-depth studies to ascertain the reasons for the stabilization of the C49 structure, the NNs still prove to be a promising test bed in which to determine the feasibility of a C49 $TiSi_2$ lithium-ion electrode. Although C49 appears to be a promising electrode candidate, reactions between Li^+ and Si, cause significant structural degradation of $TiSi_2$, leading to a loss of Ti into the electrolyte and the formation of amorphous Si on the surfaces of the NNs.[26] The previously mentioned reaction that prevented long cycle lifetimes, also made it difficult to discern whether Li^+ was incorporated into the body of $TiSi_2$ rather than the surface; without this knowledge, we were unable to rule out a competing explanation for the observed capacity—that is, surface reactions primarily compose the observed capacities of $TiSi_2$ NNs.. By preventing the degradation of the $TiSi_2$ structure, we should be able to study the system in more detail, determining which aspect of the material the observed capacity should be attributed to and the mechanism of lithiation. To achieve this goal, a thin oxide coating was formed on the surface of the $TiSi_2$ NNs; this addressed the previously noted stability issues and allowed us to determine that Li^+ reacts with Si in the bulk of $TiSi_2$ rather than

the surface. Specific capacities close to 800 mA h g^{-1} were measured (705 mA h g^{-1} at the 200th cycle), and more than 80% of the original capacity was retained after 500 cycles of repeated lithiation and delithiation. The results here are fundamentally different from previous reports from our laboratory where $TiSi_2$ NNs were used as a charge collector to improve the performance of Si nanoparticles,[9,10] as the present work focuses on understanding the intrinsic properties of $TiSi_2$.

2.3 Experimental Section

$TiSi_2$ Synthesis: $TiSi_2$ NNs were synthesized by chemical vapor deposition. Briefly, 50 standard cubic centimeters per minute (sccm) SiH_4 (10% in He), 2.5 sccm $TiCl_4$ (98%, Sigma-Aldrich), and 100 sccm H_2 (Airgas) were delivered into a heated reactor in tandem. By keeping the reactor at 675 °C and 5 Torr for 12 min, we were able to collect highly dense $TiSi_2$ NNs on a piece of Pt-coated Ti foil (Sigma). The supplies of precursors were then cut off, and the reactor was cooled to room temperature with H_2 protection. The sample was then immediately transferred into an Ar-filled glovebox (O_2 < 2 ppm, Vacuum Atmosphere Co.) for coin-cell or electrochemical cell fabrication.

$TiSi_2/SiO_2$ Synthesis: The $TiSi_2$ NNs with SiO_2 coatings were produced in the same fashion as those above, except that the reactor was opened to air at an elevated temperature of 350 °C. A layer of SiO_2 was thermally formed during the cooling process.

$TiSi_2/Al_2O_3$ Synthesis: After growth, the $TiSi_2$ NNs were transferred into the atomic layer deposition chamber immediately. Trimethylaluminum (Sigma) and water were

kept at room temperature and used as the Al and O precursors, respectively. The chamber was maintained at 200 °C during growth. The pulse time and purge time were 15 ms and 10s for both trimethylaluminum and water, respectively.

Coin Cell Fabrication: The as-synthesized samples were cut into 0.5 x 0.5 cm^2 pieces and assembled into CR2032-type coin cells with Li foils (0.38 mm, Sigma-Aldrich) by a hydraulic crimping machine (MTI) in a glovebox. $LiPF_6$ (1.0 M) in 1:1 wt/wt ethylene carbonate and diethyl carbonate (Novolyte Technologies) was used as electrolyte. Two CR2500 membranes (Celgard) were employed as separators between the two electrodes.

Electrochemical Tests: After assembly, the coin cells were kept in a home-built box at a constant temperature of 30 °C. The cycling stability was characterized by a 16-channel battery analyzer (current range: 1 μA–1A; Neware, China). The electrochemical impedance measurements were conducted using a CHI 600C potentiostat/galvanostat in an electrochemical cell. Two Li foils were used as both counter and reference electrodes, respectively. After fully lithiating or delithiating the materials at a slow charging/discharging rate (100 mA g^{-1}), we allowed the electrochemical cells to equilibrate for 2 h before collecting impedance data. The frequency was set between 50 kHz and 0.1 Hz, with a 10 mV AC amplitude. All simulations were performed used ZSimpWin.

Structural Characterization: To obtain the structural information of the NNs after testing, coin cells were opened in a glovebox and the tested electrodes were soaked in dimethoxyethane (99.5%, anhydrous, Sigma) for 24 h to remove any electrolyte. The solvent was refreshed every 4 h. The morphology was characterized by a scanning electron microscope (JEOL JSM-6340) and a transmission electron microscope (JEOL JEM-2010F).

Electron Energy Loss Spectroscopy: Electron energy loss spectroscopy measurements were conducted for both unlithiated and lithiated samples. The measurements were conducted on a JEM-2010F equipped with a parallel detection EELS spectrometer.

2.4 Results and Discussion

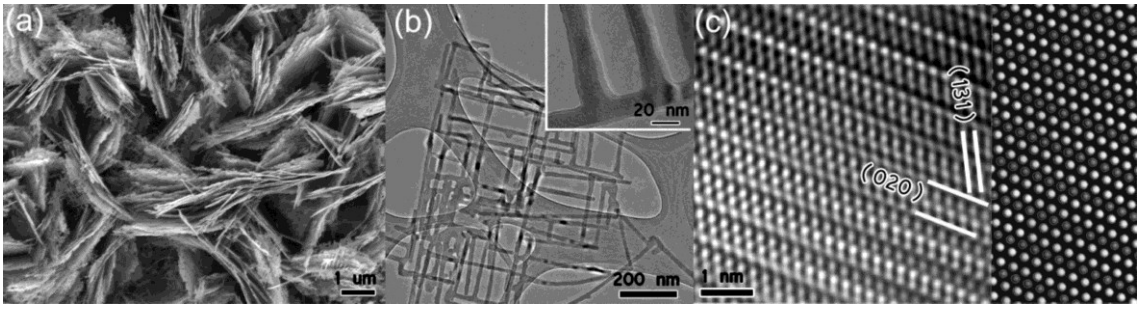

Figure 2.2. An examination of the oxide-coated $TiSi_2$ NNs. (a) A SEM micrograph demonstrating the structural purity of the NN synthesis. In this instance, purity is used to refer to the lack of non-NN structures, e.g., rods, tubes, or wires, in the NN synthesis. (b) A low-magnification TEM micrograph that demonstrates the connectivity of the individual beams in the NN structure. The inset shows the oxide layer clearly. (c) A high-resolution TEM image viewed along the {020} plane is presented in this panel. The experimental image (left) matches the simulated image (right), confirming the $TiSi_2$ is, indeed, C49 $TiSi_2$. Reprinted with permission from *ACS Nano.*, **2012**, *6* (9), 8114-8119. **Copyright 2012 American Chemical Society.**

The $TiSi_2$ NNs utilized for the experiments performed in this chapter were obtained via the CVD reaction between $TiCl_4$ and SiH_4 in a H_2-rich environment. A moderate growth temperature of 675 °C and a short growth time of 12 min yield a dense deposition; the average areal density of the synthesis was approximately 100 μg cm^{-2}. To form a conformal oxide overlayer, as-synthesized $TiSi_2$ NNs were exposed to ambient air at 350 °C and allowed to cool to room temperature naturally. Figure 2.2 includes a TEM micrograph in the inset, demonstrating that the coating was 4 nm in thickness and amorphous in nature. To determine whether any beneficial effects were bestowed upon the system irrespective to the deposition method of the oxide coating, oxide coatings were deposited via other methods, e.g., atomic layer deposition, to serve the purpose of stabilizing $TiSi_2$ almost as well as the amorphous coatings.

Oxide-coated $TiSi_2$ NNs produced according to the abbreviated procedure in the previous paragraph were tested using a two electrode coin cell for charge and discharge characterizations or a three-electrode electrochemical cell for impedance studies. Representative charge and discharge behaviors are plotted in Figure 2.3a and b. In the first cycle, a significant portion of the electrons that passed through the electrode were consumed in irreversible reactions, e.g., the formation of an SEI layer, as evidenced by the disparity between the charge step with a lithiation capacity of 3045 mA h g^{-1} and discharge step with a delithiation capacity of 943 mA h g^{-1}. Similar behaviors have also been frequently reported in other systems, although the exact nature of the irreversible processes remains unclear at this stage.[27] With continued cycling, the coulombic

efficiency increased and the disparity between charge and discharge curves disappeared after the first five cycles. Figure 2.3b demonstrates the stability of the oxide-coated $TiSi_2$ NNs between the sixth and ninth cycles at a charge/discharge rate of 2000mA g^{-1}; the similarity of the overlapping curves is indicative of the stability of the system in this instance. Consistent with the plots, the calculated coulombic efficiencies were greater than 98%. Note that due to the limited data sampling capability at the relatively fast charge and discharge rates of 2000 mA g^{-1} exhibited by the battery analyzer (BTS-5 V1 mA, Neware, China) utilized in the cycling tests, the coulombic efficiencies listed herein may be systematically underestimated.

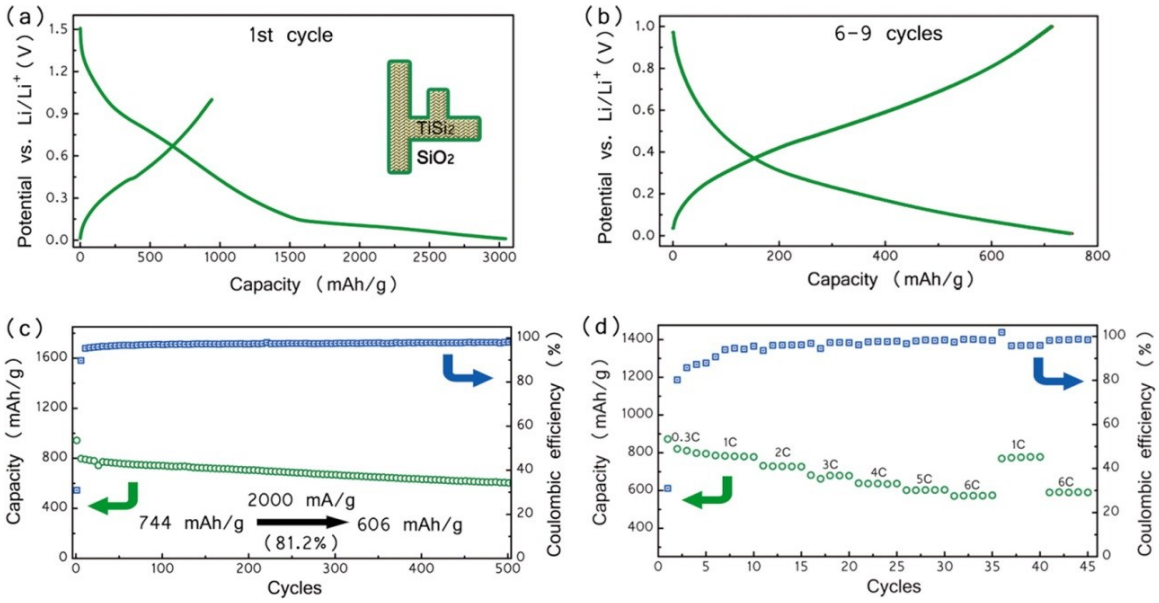

Figure 2.3. Electrochemical profiles of oxide-coated $TiSi_2$ NNs. (a) Charge/discharge characteristics of the first charge and discharge cycle. The cycling parameters are as follows: rate: 200 mA g^{-1}; potential range: 1.5 to 0.01 V. (b) Charge/discharge characteristics of the cycles 6 through 9. The traces overlap well, demonstrating the stability of the electrode. The cycling parameters are as follows: rate: 2000 mA g^{-1}; potential range: 1.0 to 0.01 V. (c) A chart plotting the capacity of the battery over cycles 0 to 500 on the left y axis and the coulombic efficiency for cycles 0 to 500 on the right y axis. For this test, the rate was 2000 mA g^{-1} with a potential range of 1.0 to 0.01 V. (d) Rate-dependent specific capacities of the oxide-coated

$TiSi_2$ electrode. The cell was cycled between 1.0 and 0.01 V, and a rate of 1C is equivalent to 1029 mA g^{-1}. Reprinted with permission from *ACS Nano.*, **2012**, *6* (9), 8114-8119. **Copyright 2012 American Chemical Society.**

While the sufficient overlap demonstrated between the charge and discharge curves in 3 cycles is indicative of the short-term cycling stability of a battery, observation during an increased number of cycles is necessary to determine the long-term cycling stability of an electrode material. Figure 2.3c contains the charge and discharge behaviors of the system when the charge and discharge tests were extended to 500 cycles. For this group of data, the first five cycles were carried out at a rate of 200 mA g^{-1} in order to condition the electrode; this rate was increased by 10-fold to a rate of 2000 mA g^{-1} for all subsequent cycles. In order to present the data in a more uncluttered fashion we have opted to display one data point every five cycles. The capacity decreased from 744 mA h g^{-1} at the 26th cycle to 606 mA h g^{-1} at the 500th cycle, corresponding to an overall capacity loss of 18.8%, or 0.04% $cycle^{-1}$.

The rate performance of $TiSi_2$ is noteworthy. For a measured capacity of 744 mA h g^{-1} at a rate of 2000 mA g^{-1}, a charge or discharge process takes approximately 22 min. This excellent rate performance is enabled by the good electrical conductivity of $TiSi_2$: approximately 105 S cm^{-1}. Through the employed synthesis of the $TiSi_2$ NNs, an intimate contact between the nets and the underlying substrate, which also acts as a conductive charge collector, is formed, making the use of additional conductive binders unnecessary. The gaps between the beams of individual $TiSi_2$ NNs, typically larger than 50 nm, are expected to enable fast electrolyte diffusion as well. Figure 2.3d plots how

the capacity changed as the charge rates were varied between 0.3C and 6C, if we define 1C as 1029 ma g^{-1}. At 6C (6174mA g^{-1}), the measured capacity was 574mA h g^{-1}, corresponding to 74% of the value at 0.3C. Remarkably, more than 99.9% of the initial capacity was recovered when the cell was again measured at 1C.

To calculate the value of 1029 mA g^{-1} that we used for 1C, we utilized the structure depicted in Figure 2.1c and assumed that only the Si layer contributes to the capacity of the electrode. We also assumed that each Si atom can host 4 Li^{+}, leading to a lithiated formula of Li_4TiSi_2 and, hence, a specific capacity of 1029 mA h g^{-1}. Of course, while this coarse approximation predicts a capacity that is close to the capacity of 943 mAh g^{-1} demonstrated by the electrode, it lacks a theoretical basis and, as such, should be used only as a general reference.

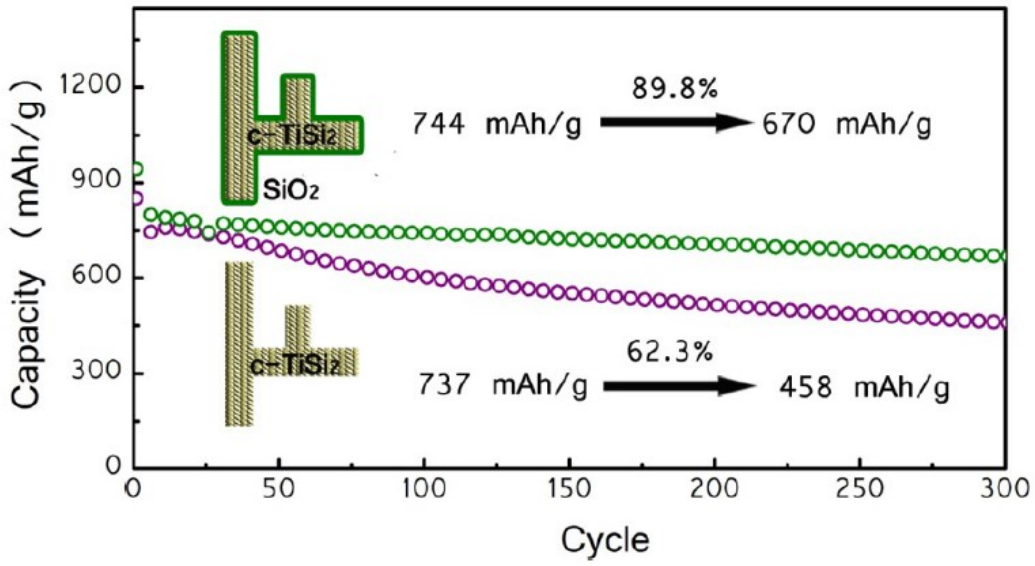

Figure 2.4. A comparison of oxide-coated $TiSi_2$ NNs and as-grown $TiSi_2$ NNs. The capacities of both oxide-coated (green) and as-grown (purple) were plotted against their respective cycle numbers. From the 26th to 300th cycles, SiO_2-coated NNs lost 10.2% of their 26th cycle capacity,

whereas the unprotected NNs lost 37.7% of their 26th cycle capacity. The stability conferred by a protective oxide coating is highlighted by these results. Reprinted with permission from *ACS Nano.*, **2012**, *6* (9), 8114-8119. **Copyright 2012 American Chemical Society.**

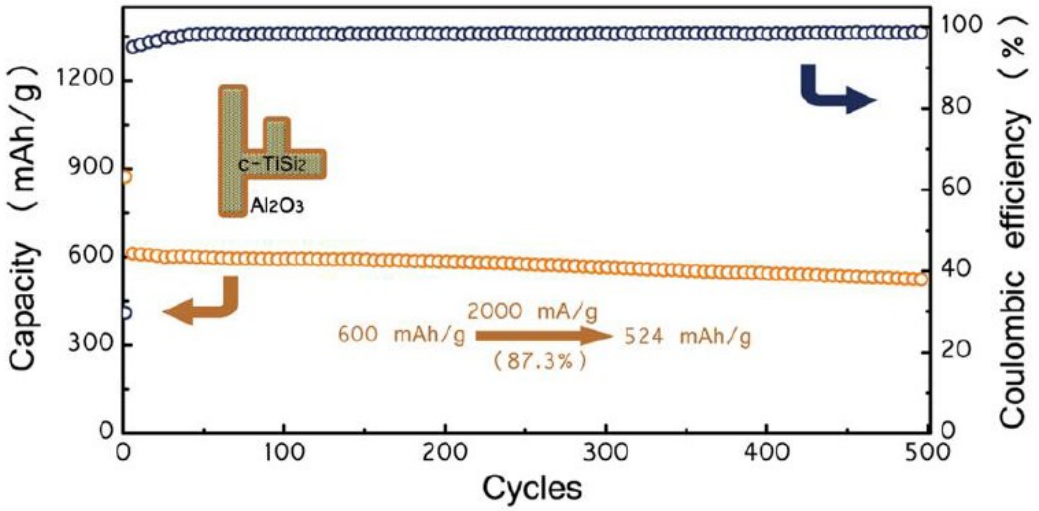

Figure 2.5. The cycling stability of a NN protected with an oxide other than thermally formed SiO_2. In this case, the NN was protected with a 1 nm thick coating of Al_2O_3 deposited via ALD. After 500 cycles, only 12.7% of the initial capacity is lost. The capacity of the Al_2O_3-coated sample is lower than those of the uncoated or SiO_2-coated NN samples. Reprinted with permission from *ACS Nano.*, **2012**, *6* (9), 8114-8119. **Copyright 2012 American Chemical Society.**

Although the electrode material demonstrates good performance characteristics, it must be reiterated that the oxide that has been formed on the surface of the electrode is invaluable to the performance of the $TiSi_2$ anode. When charge and discharge tests are performed on oxide-free $TiSi_2$ samples, the capacity fades at a rate more than double that of an oxide-coated sample; this behavior is demonstrated in Figure 2.4 and Figure 2.5. The effect of an oxide coating has been discussed by other authors as well.[28-33] Some groups believe an oxide coating, when sufficiently thin, is permeable to ions, in this case Li^+, but blocks electron transfer, preventing the occurrence of side reactions

that degrade electrode performance. The oxide layer, in essence, acts as a desired SEI or serves to facilitate SEI formation.[28] Others have proposed that oxides, SiO_2 in particular, may participate in the charge and discharge processes by reacting with Li^+ to form Li_xO and SiO_x, where $x < 2$.[34-36] In order to understand the nature of the improved performance imparted by an oxide coating, we carried out EIS measurements. The data for oxide-stabilized $TiSi_2$ in fully lithiated and delithiated forms are shown in Figure 2.4, and they should be compared to previous work from our laboratory where EIS measurements of oxide-free $TiSi_2$ were reported.[26] A fundamental difference is observed in the impedance after delithiation. For $TiSi_2$ samples lacking an oxide coating, a drastic increase of impedance typically accompanied the delithation process; this behavior is attributed to changes in the SEI layer induced by lithiation and delithiation reactions.[27,37] Such an impedance change was largely absent in the oxide-stabilized $TiSi_2$ (Figure 2.6). This result implies that the oxide coating alters the nature of and the formation of the SEI layer. The oxide coating also has a second purpose—it acts a mechanical constraint that prevents the exfoliation of layered $TiSi_2$ during lithiation,[29,33,38] which would otherwise lead to an eventual mechanical breakdown of the electrode material and a resulting loss of capacity. Taken as a whole, the improved SEI and the mechanical protection conferred by an oxide coating enable significantly enhanced cyclability of $TiSi_2$. In addition, by fitting the lithiated data, the charge transfer resistance was found to be only approximately 100 Ω, indicating that although the $TiSi_2$ is coated with an insulating material, the NNs still demonstrate good charge conduction

(Figure 2.7). While it is clear that adding an oxide layer to the system is beneficial to the stability of the anode, it is not clear whether the conferred stability is solely due to properties of the oxide or due to the possible modification of the SEI layer. Therefore, further work needs to be conducted to clarify this matter.

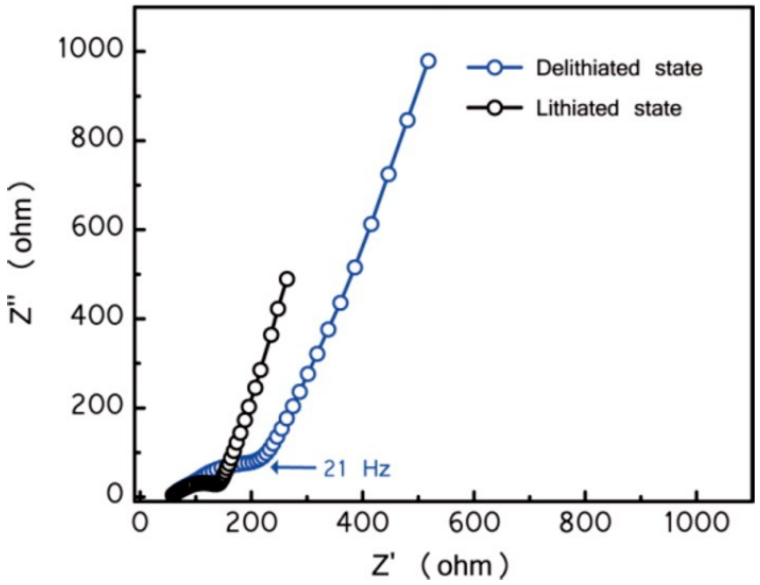

Figure 2.6. Electrochemical impedance spectra of oxide-stabilized $TiSi_2$ NNs. A sample was fully lithiated to a potential of 0.01 V at a rate of 100 mA g^{-1}. The sample was then allowed to reach equilibrium for 2 h before impedance data were collected. The frequency was swept between 50 kHz to 1 Hz, with an AC amplitude of 10 mV. After collected the lithiated state spectrum, the sample was fully delithiated to 1.0 V at a rate of 100 mA g^{-1}. After delithiation, the impedance data were collected using the same 50 kHz to 1 Hz range with an amplitude of 10 mV. Reprinted with permission from *ACS Nano.*, **2012**, *6* (9), 8114-8119. **Copyright 2012 American Chemical Society.**

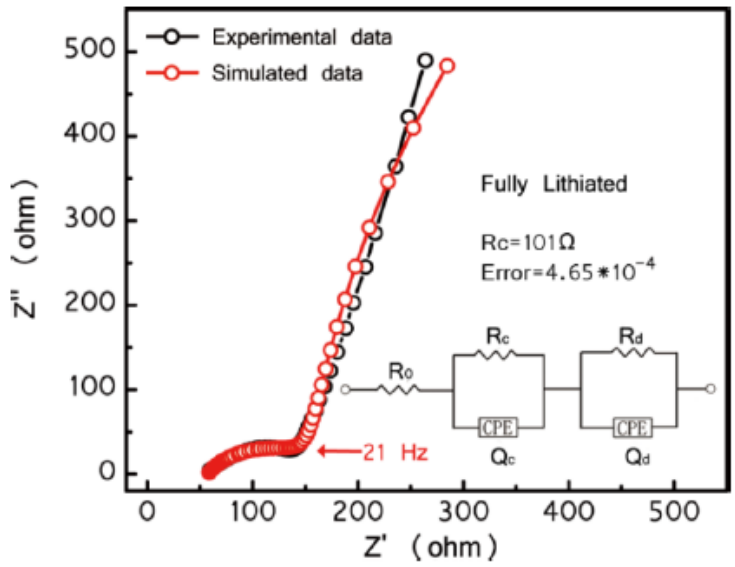

Figure 2.7. The electrochemical impedance spectrum of SiO_2-coated $TiSi_2$ NNs in Nyquist plot form. The Nyquist plot of a fully lithiated sample is depicted here, accompanied by a simulated spectrum generated by the inset equivalent electric circuit. The spectra comprise a semi-circle and an inclined line. From these shapes, the information pertaining to charge transfer and Li^+ diffusion in the electrode can be extracted. Reprinted with permission from *ACS Nano.*, **2012**, *6* (9), 8114-8119. **Copyright 2012 American Chemical Society.**

The claim that Li^+ inserts into the Si-only layers in $TiSi_2$ is one that requires evidence. In this section, that evidence is presented. We begin with the assumption that the observed capacity results from reactions between Si and Li^+ because there are no known reactions between Ti and Li. If Li^+ is being incorporated into the Si-only layers of $TiSi_2$, a subsequent increase of the lattice spacing of the {020} planes should occur. Indeed, When the lattice spacings of the {020} planes were compared before and after lithiation, we observed an increase from 0.667 to 0.675 nm, corresponding to a 1.2% change; no other measurable differences were observed along other crystal planes (Figure2.8). This small but non-negligible change indicates the insertion of Li^+ into the {020} planes, where Si-only layers reside. To verify that Li^+ was incorporated into the $TiSi_2$ after

lithiation, EELS was employed; the results confirm the presence of Li in the lithiated sample, as shown in Figure 2.9d. There is a distinct lack of a signal attributable to the presence of Li in as-grown $TiSi_2$ samples, as expected (Figure 2.9c). The combination of lattice spacing changes in addition to the verification of the presence of Li after lithiation support the proposed mechanism of Li incorporation into the Si-only layers of $TiSi_2$. The small changes in volume upon Li^+ insertion and extraction also lead to better cycling stability in the layered-structure $TiSi_2$ when compared to Si-based alloy anodes. Additionally, the NN morphology and crystalline nature are well preserved after 100 cycles (Figure 2.10).

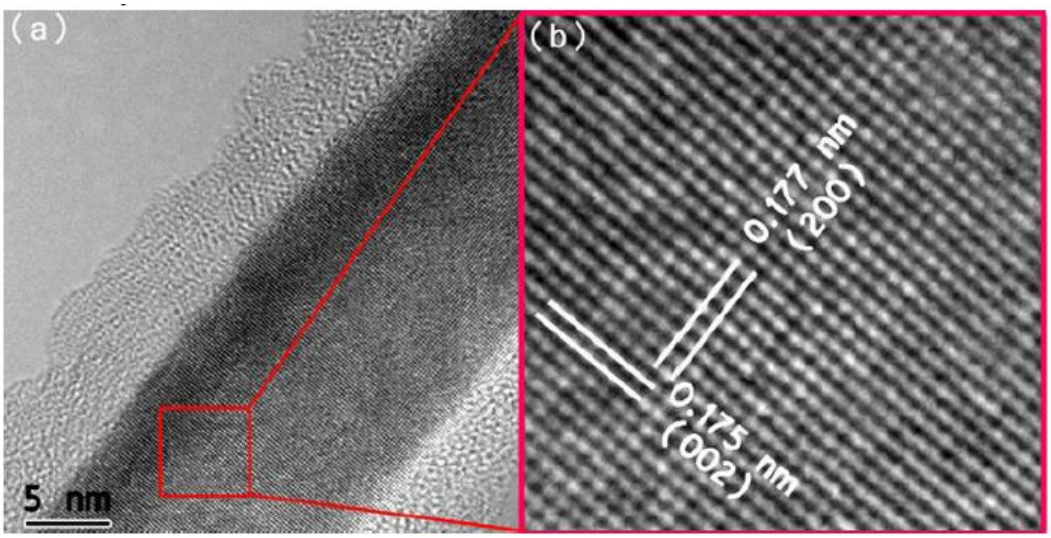

Figure 2.8. TEM images of fully-lithiated $TiSi_2$ NNs. (a) A low-magnification image highlighting the intact beam of a NN after lithiation to 0.01 V. (b) A high-resolution TEM micrograph demonstrating that the lattice of $TiSi_2$ along the [002] and [200] directions does not exhibit obvious expansion upon full lithiation. Reprinted with permission from *ACS Nano.*, **2012**, *6* (9), 8114-8119. **Copyright 2012 American Chemical Society.**

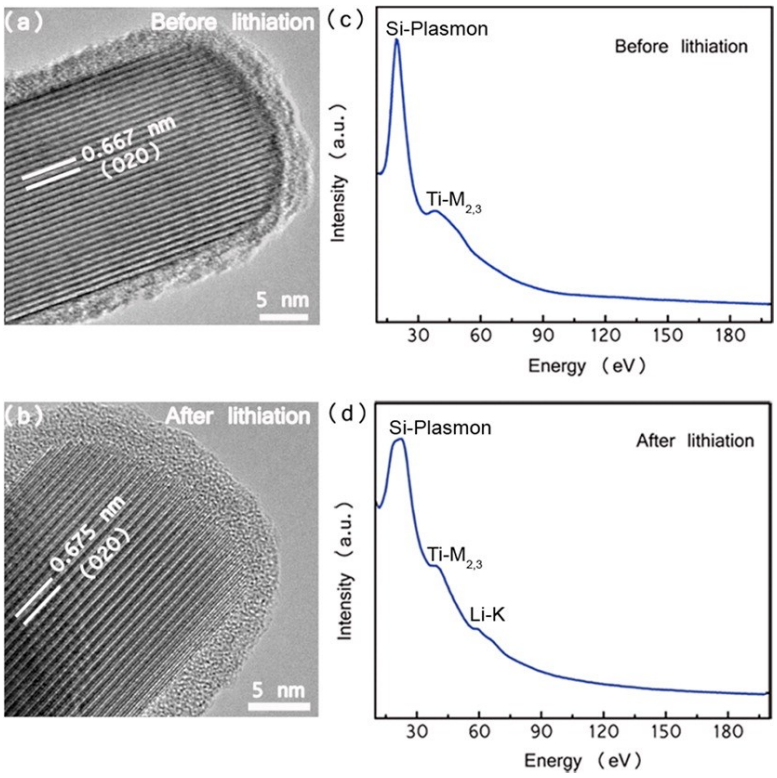

Figure 2.9. High-resolution TEM images of $TiSi_2$ before (a) and after (b) lithiation. (c and d) Electron energy loss spectroscopy results of single $TiSi_2$ NNs before (c) and after (d) lithiation. Reprinted with permission from *ACS Nano.*, **2012**, *6* (9), 8114-8119. **Copyright 2012 American Chemical Society.**

Ideally, powder XRD patterns taken before lithiation and at various stages of charge and discharge would be useful in the task of elucidating the lithiation mechanism of $TiSi_2$. However, in this situation, specific limitations preclude the use of powder XRD data. On the basis of the observed d-spacing change presented in Figure 2.8, the shift in the (020) peak position would be 0.16°; this shift is based on the calculated values of 13.27° and 13.11° 2θ (Cu Kα). In addition to the small peak shift, the (020) peak is not present in XRD diffraction patterns collected from as-grown $TiSi_2$ NNs.[39] The broadening of the diffraction peak due to the small size of the nets would also complicate matters.

Finally, the (060) peak could possibly be used, but it is partially eclipsed by the presence of the (131) peak.[39]

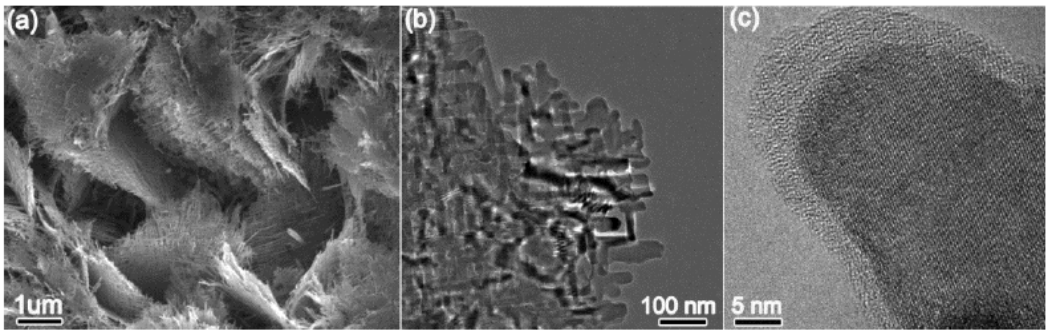

Figure 2.10. Electron micrographs of SiO_2-coated $TiSi_2$ after 100 cycles of lithiation and delithiation. (a) A SEM micrograph highlighting the densely packed NNs on the Ti growth substrate. (b) A low magnification TEM image verifying the preservation of the NN structure after repeated lithiation and delithiation. (c) A high-resolution TEM micrograph demonstrates that the NNs are still crystalline after 100 cycles. Reprinted with permission from *ACS Nano.*, **2012**, *6* (9), 8114-8119. **Copyright 2012 American Chemical Society.**

2.5 Conclusion

In the case of electrochemical devices, their performance is intimately reliant upon the properties of their individual components; electrochemical performance characteristics rely particularly heavily upon the electrodes. With the discovery of new electrode compounds or mechanism, advancements in storage technology can occur. It is within this context that we believe our results are significant. The $TiSi_2$ NNs, which are of the C49 crystal structure, represent a rare example of a layered, non-graphitic anode material. This study was enabled by our strategy to stabilize layered $TiSi_2$ NNs using an easy-to-implement oxide coating formed by the simple exposure to air while the electrode was at elevated temperatures. The stabilized material survives up to 500

cycles of lithiation and delithiation, enabling the possibility of the material's application as an electrode in lithium ion batteries. The stabilization also allowed us to perform detailed structural studies to confirm that Li ions are indeed reversibly inserted and extracted from the Si-only layer in $TiSi_2$ NNs. This simple structure opens a doorway to significantly improved energy storage devices in terms of cyclability and power rate.

2.6 References

1. Tarascon, J. M.; Armand, M., Issues and challenges facing rechargeable lithium batteries. *Nature* **2001**, *414*, 359-367.
2. Rao, B. M. L.; Francis, R. W.; Christopher, H. A., Lithium-aluminum electrode. *J. Electrochem. Soc.* **1977**, *124*, 1490-1492.
3. Boukamp, B. A.; Lesh, G. C.; Huggins, R. A., All-solid lithium electrodes with mixed-conductor matrix. *J. Electrochem. Soc.* **1981**, *128*, 725-729.
4. Chan, C. K.; Peng, H.; Liu, G.; McIlwrath, K.; Zhang, X. F.; Huggins, R. A.; Cui, Y., High-performance lithium battery anodes using silicon nanowires. *Nat. Nano* **2008**, *3*, 31-35.
5. Whittingham, M. S., Electrical energy storage and intercalation chemistry. *Science* **1976**, *192*, 1126-1127.
6. Mizushima, K.; Jones, P. C.; Wiseman, P. J.; Goodenough, J. B., Li_xCoO_2 ($0 < x \leq 1$): a new cathode material for batteries of high energy density. *Mater. Res. Bull.* **1980**, *15*, 783-789.
7. Zhou, S.; Liu, X.; Lin, Y.; Wang, D., Spontaneous growth of highly conductive two-dimensional single-crystalline $TiSi_2$ nanonets. *Angew. Chem., Int. Ed.* **2008**, *47*, 7681-7684.
8. Lin, Y.; Zhou, S.; Sheehan, S. W.; Wang, D., Nanonet-based hematite heteronanostructures for efficient solar water splitting. *J. Am. Chem. Soc.* **2011**, *133*, 2398-2401.
9. Zhou, S.; Liu, X.; Wang, D., $Si/TiSi_2$ heteronanostructures as high-capacity anode material for Li ion batteries. *Nano Lett.* **2010**, *10*, 860-863.
10. Xie, J.; Yang, X.; Zhou, S.; Wang, D., Comparing one- and two-dimensional heteronanostructures as silicon-based lithium ion battery anode materials. *ACS Nano* **2011**, *5*, 9225-9231.
11. Zhou, S.; Yang, X.; Lin, Y.; Xie, J.; Wang, D., A nanonet-enabled Li ion battery cathode material with high power rate, high capacity, and long cycle Lifetime. *ACS Nano* **2011**, *6*, 919-924.
12. Ozawa, K., Lithium-ion rechargeable batteries with $LiCoO_2$ and carbon electrodes: the $LiCoO_2$/C system. *Solid State Ionics* **1994**, *69*, 212-221.
13. Armand, M.; Tarascon, J. M., Building better batteries. *Nature* **2008**, *451*, 652-657.

14. Kim, H.; Han, B.; Choo, J.; Cho, J., Three-dimensional porous silicon particles for use in high-performance lithium secondary batteries. *Angew. Chem., Int. Ed. Engl.* **2008**, *47*, 10151-10154.
15. Hu, Y.-S.; Demir-Cakan, R.; Titirici, M.-M.; Müller, J.-O.; Schlögl, R.; Antonietti, M.; Maier, J., Superior storage performance of a Si@SiO_x/C nanocomposite as anode material for lithium-ion batteries. *Angew. Chem., Int. Ed. Engl.* **2008**, *47*, 1645-1649.
16. Kasavajjula, U.; Wang, C.; Appleby, A. J., Nano- and bulk-silicon-based insertion anodes for lithium-ion secondary cells. *J. Power Sources* **2007**, *163*, 1003-1039.
17. Wolfenstine, J., $CaSi_2$ as an anode for lithium-ion batteries. *J. Power Sources* **2003**, *124*, 241-245.
18. Liu, W.-R.; Wu, N.-L.; Shieh, D.-T.; Wu, H.-C.; Yang, M.-H.; Korepp, C.; Besenhard, J. O.; Winter, M., Synthesis and characterization of nanoporous NiSi-Si composite anode for lithium-ion batteries. *J. Electrochem. Soc.* **2007**, *154*, A97-A102.
19. Roberts, G. A.; Cairns, E. J.; Reimer, J. A., Magnesium silicide as a negative electrode material for lithium-ion batteries. *J. Power Sources* **2002**, *110*, 424-429.
20. Deng, D.; Lee, J. Y., Reversible storage of lithium in a rambutan-like tin–carbon electrode. *Angew. Chem., Int. Ed. Engl.* **2009**, *48*, 1660-1663.
21. Yu, Y.; Gu, L.; Wang, C.; Dhanabalan, A.; van Aken, P. A.; Maier, J., Encapsulation of Sn@carbon nanoparticles in bamboo-like hollow carbon nanofibers as an anode material in lithium-based batteries. *Angew. Chem., Int. Ed. Engl.* **2009**, *48*, 6485-6489.
22. Park, M.-S.; Wang, G.-X.; Kang, Y.-M.; Wexler, D.; Dou, S.-X.; Liu, H.-K., Preparation and electrochemical properties of SnO_2 nanowires for application in lithium-ion batteries. *Angew. Chem., Int. Ed. Engl.* **2007**, *46*, 750-753.
23. Paek, S.-M.; Yoo, E.; Honma, I., Enhanced cyclic performance and lithium storage capacity of SnO_2/graphene nanoporous electrodes with three-dimensionally delaminated flexible structure. *Nano Lett.* **2008**, *9*, 72-75.
24. Beyers, R.; Sinclair, R., Metastable phase formation in titanium-silicon thin films. *J. Appl. Phys.* **1985**, *57*, 5240-5245.
25. Netz, A.; Huggins, R. A.; Weppner, W., Investigations of a number of alternative negative electrode materials for use in lithium cells. *Ionics* **2001**, *7*, 433-439.
26. Zhou, S.; Wang, D., Unique lithiation and delithiation processes of nanostructured metal silicides. *ACS Nano* **2010**, *4*, 7014-7020.
27. Chan, C. K.; Ruffo, R.; Hong, S. S.; Cui, Y., Surface chemistry and morphology of the solid electrolyte interphase on silicon nanowire lithium-ion battery anodes. *J. Power Sources* **2009**, *189*, 1132-1140.
28. Xiao, X.; Lu, P.; Ahn, D., Ultrathin multifunctional oxide coatings for lithium ion batteries. *Adv. Mater.* **2011**, *23*, 3911-3915.
29. Cho, J.; Kim, Y. J.; Kim, T.-J.; Park, B., Zero-strain intercalation cathode for rechargeable Li-ion cell. *Angew. Chem., Int. Ed. Engl.* **2001**, *40*, 3367-3369.
30. Kim, J.-S.; Johnson, C. S.; Vaughey, J. T.; Hackney, S. A.; Walz, K. A.; Zeltner, W. A.; Anderson, M. A.; Thackeray, M. M., The electrochemical stability of spinel electrodes coated with ZrO_2, Al_2O_3, and SiO_2 from colloidal suspensions. *J. Electrochem. Soc.* **2004**, *151*, A1755-A1761.
31. Fan, Y.; Wang, J.; Tang, Z.; He, W.; Zhang, J., Effects of the nanostructured SiO_2 coating on the performance of $LiNi_{0.5}Mn_{1.5}O_4$ cathode materials for high-voltage Li-ion batteries. *Electrochim. Acta* **2007**, *52*, 3870-3875.

32. Fu, L. J.; Liu, H.; Li, C.; Wu, Y. P.; Rahm, E.; Holze, R.; Wu, H. Q., Surface modifications of electrode materials for lithium ion batteries. *Solid State Sci.* **2006**, *8*, 113-128.
33. Zhang, T.; Gao, J.; Zhang, H. P.; Yang, L. C.; Wu, Y. P.; Wu, H. Q., Preparation and electrochemical properties of core-shell Si/SiO nanocomposite as anode material for lithium ion batteries. *Electrochem. Commun.* **2007**, *9*, 886-890.
34. Sun, Q.; Zhang, B.; Fu, Z.-W., Lithium electrochemistry of SiO_2 thin film electrode for lithium-ion batteries. *Appl. Surf. Sci.* **2008**, *254*, 3774-3779.
35. Miyachi, M.; Yamamoto, H.; Kawai, H.; Ohta, T.; Shirakata, M., Analysis of SiO anodes for lithium-ion batteries. *J. Electrochem. Soc.* **2005**, *152*, A2089-A2091.
36. Abel, P. R.; Lin, Y.-M.; Celio, H.; Heller, A.; Mullins, C. B., Improving the stability of nanostructured silicon thin film lithium-ion battery anodes through their controlled oxidation. *ACS Nano* **2012**, *6*, 2506-2516.
37. Ruffo, R.; Hong, S. S.; Chan, C. K.; Huggins, R. A.; Cui, Y., Impedance analysis of silicon nanowire lithium ion battery anodes. *J. Phys. Chem. C* **2009**, *113*, 11390-11398.
38. Wu, H.; Chan, G.; Choi, J. W.; Ryu, I.; Yao, Y.; McDowell, M. T.; Lee, S. W.; Jackson, A.; Yang, Y.; Hu, L.; Cui, Y., Stable cycling of double-walled silicon nanotube battery anodes through solid-electrolyte interphase control. *Nat Nano* **2012**, *7*, 310-315.
39. Zhou, S.; Liu, X.; Lin, Y.; Wang, D., Rational synthesis and structural characterizations of complex $TiSi_2$ nanostructures. *Chem. Mater.* **2009**, *21*, 1023-1027.